Fully consistent modeling of dike induced deformation and seismicity: Application to the 2014 Bárðarbunga dike, Iceland

Elías R. Heimisson[1], **Paul Segall**[1]

[1]Department of Geophysics, Stanford University, Stanford, California, USA

Key Points:

- The model presented captures the complex space-time history of seismicity and deformation.
- Results are consistent with dike induced earthquake being triggered on preexisting faults.
- Results suggest a wider applicability of the Dieterich 1994 theory than previously explored.

Corresponding author: Elías R. Heimisson, `eliasrh@stanford.edu`

Abstract

Dike intrusions are often associated with surface deformation and propagating swarms of earthquakes. These are understood to be manifestations of the same underlying physical process, although rarely jointly modeled. In this paper, we construct a physics-based model of the 2014 Bárðarbung dike, by far the best observed large dike (> 0.5 km^3) to date. We constrain the background stress state by the total dike deformation, time-dependent dike pressure from continuous GPS and seismicity, and the spatial dependence of frictional properties via the space-time evolution of seismicity. We find that the geodetic and earthquake data can be reconciled with a set of self-consistent parameters. We show that the complicated spatial and temporal evolution of the Bárðarbunga seismicity can be explained through dike induced elastic stress changes on preexisting faults, constrained by observed focal mechanisms. In particular, the model captures the segmentation of the seismicity, where only the newest dike segment remains seismically active. Dike pressure drops during rapid advances and builds up during pauses. Our results indicate that many features in the seismicity result from the interplay between time-dependent pressure and stress memory effects. The spatial variability in seismicity requires heterogeneity in frictional properties and/or local initial stresses. Finally, the methodology presented outlines a new approach to quantitative integration of seismic and geodetic data and may be applied to a broader class of problems.

1 Introduction

Seismicity and deformation have long been successfully used to study volcanic processes, as well as other dynamic crustal processes. Yet, most studies do not jointly interpret or model the two types of data quantitatively, although they are usually considered signatures of the same underlying process. Modeling deformation in volcanic settings on short time scales where elastic deformation dominates is reasonably well understood. However, modeling of earthquake production or seismicity rate is currently much less well understood. To gain further insight and understanding into dynamic, and sometimes life-threatening, earth processes we seek to develop quantitative models that are consistent with more than one independent observation. The goal of this study is to develop such a model and apply it to the 2014 Bárðarbunga dike intrusion with fully consistent deformation and stress fields that affect both data types. A consistent mechanical framework for analyzing both deformation and seismic data could potentially lead to improved, physics-based eruption forecasts.

Our study may be regarded as a hypothesis test; we test if a physics-based dike model constrained by geodetic observations can be reconciled with the complex spatial and temporal evolution of seismicity during the 2014 Bárðarbunga diking event using an earthquake production constitutive law based on rate-and-state friction [*Dieterich*, 1994; *Heimisson and Segall*, 2018]. Specifically, we hypothesize that seismicity is triggered on prestressed faults that host a population of seismic sources with heterogeneous initial conditions. Due to the complexity of the stressing history, the magnitude of the stresses involved, and the resulting complex seismic behavior, these observations offer a much more stringent test of the validity of the rate-and-state based models of earthquake production than have been explored in previous studies of aftershocks, where stress magnitudes are frequently smaller and temporal changes in stresses are simpler than in this study. Our findings suggest that these models are in general agreement with observation, thus further validating the use of rate-and-state constitutive relationship for earthquake production for more complicated stressing histories and in different settings then have previously been explored.

As a dike propagates it deforms the crust and causes dramatic stress changes in the near field; this usually results in the dike inducing a propagating swarm of seismicity. It is generally thought that the leading edge of the seismicity marks the approximate location of the dike tip since that is where the local stresses are largest. The September 1977 Krafla, Iceland dike intrusion provides convincing and unique evidence for the propagating swarm of seismicity being produced near the dike tip. Dike propagation was marked by a swarm of seismicity that migrated ~ 8 km from the center of the Krafla caldera and intersected a geothermal borehole [*Brandsdottir and Einarsson*, 1979]. A small volume of basaltic tephra was erupted from the borehole [*Larsen and Grönvold*, 1979], shortly after the earthquakes propagated into the vicinity of the well. However, the exact mechanism of the dike induced seismicity is not well understood. More generally, the relationship between processes that stress and deform the Earth's crust and the resulting triggered or induced seismicity is still a subject of active research. Dike intrusions offer a unique tool to investigate this problem since they often produce large numbers of earthquakes and significant deformation that evolves on easily resolvable timescales.

Most modeling of dike intrusions apply kinematic dislocation models [e.g. *Du and Aydin*, 1992; *Jónsson et al.*, 1999; *Sigmundsson et al.*, 2015; *Green et al.*, 2015], which typically utilize the analytical solutions for finite dislocations in elastic, isotropic half-space [e.g., *Okada*, 1992]. Sometimes these models are subject to ad hoc regularization to smooth the opening where the degree of smoothing is based on signal to noise ratio of the data, not on the physics of pressurized cracks in elastic solids. A different approach to modeling magmatic intrusions is to derive opening from traction boundary conditions [e.g. *Cayol and Cornet*, 1998; *Sigmundsson et al.*, 2010; *Hooper et al.*, 2011; *Segall et al.*, 2013], this is referred to as a magmastatic crack model since viscous stresses in the fluid are neglected. This approach greatly reduces the number of free parameters and results in a smoothly varying opening corresponding to a fluid-filled crack in static equilibrium with the elastic crust. The added benefit of this approach is that it can yield more realistic stress fields surrounding the dike, whereas kinematic dislocation models fail to accurately represent the near field stresses imposed by the dike.

Segall et al. [2013] took the first steps toward a quantitative analysis of triggering of microseismicity during dike propagation and surface deformation. They performed a joint inversion of data from the "Father's Day" intrusion in Kilauea, where a boundary element crack model based on elastic Green's function related opening to surface displacements and changes in tractions in volume elements (voxels). From the predicted shear and normal tractions, inside each voxel, the cumulative number of events was computed using the *Dieterich* [1994] seismicity rate theory. In a broad sense, we follow the same approach as *Segall et al.* [2013], applied to the Bárðarbunga dike. Since the Bárðarbunga dike is geometrically and temporally more complicated than the "Father's Day" intrusion the specific implementation of the *Segall et al.* [2013] approach cannot be applied directly to these data. Here we outline some methodological changes to the approach of *Segall et al.* [2013]. This includes computing the predicted number of earthquakes based on the integral formulation of *Heimisson and Segall* [2018], and adapting the problem to a non-planar dike geometry by spatial discretization of earthquakes and fault tractions within tetrahedra voxels. The dike here evolves vertically, as well as laterally, in a realistic tectonic stress environment, whereas the height of the Fathers Day dike was fixed. In addition, a different computational approach is taken where elastic Green's functions are only evaluated once and then stored, such that they are not evaluated during optimization, which tends to be very computationally expensive. Furthermore, the Bárðarbunga dike was a much larger dike than Father's Day intrusion with a more complicated spatial and temporal evolution, which consequently has resulted in a much richer and more complete data set. For example, the Bárðarbunga dike was monitored by nearly a dozen continuous GPS stations (Figure 1), InSAR acquisition, and a dense seismic network which was used to locate over 30,000 events with high accuracy [*Ágústsdóttir et al.*, 2016]. In contrast, the Father's Day intrusion only had a few hundred detected events. Another important distinction is that this study explores what conditions are needed to explain the rich Bárðarbunga dataset, specifically the dike seismicity, whereas *Segall et al.* [2013] directly used a combination of seismic and geodetic data to constrain the dike length and pressure.

1.1 The 2014 Bárðarbunga dike, Iceland

The 2014 Bárðarbunga dike is by far the best instrumented large dike intrusion to date, with more than 30,000 detected earthquakes [*Ágústsdóttir et al.*, 2016]. Furthermore, a large deformation signal was observed by continuous GPS and a number of InSAR acquisitions [*Sigmundsson et al.*, 2015]. The high-quality data led to many interesting observations: The seismicity was mostly concentrated in a limited depth range of 5 – 7 km, and was focused on the actively intruding segment [*Ágústsdóttir et al.*, 2016]; The trajectory of the dike had several abrupt turns; propagation often halted before changing direction; During these halts, the dike inflated (based on continuous GPS data), implying it accumulated magma [*Sigmundsson et al.*, 2015].

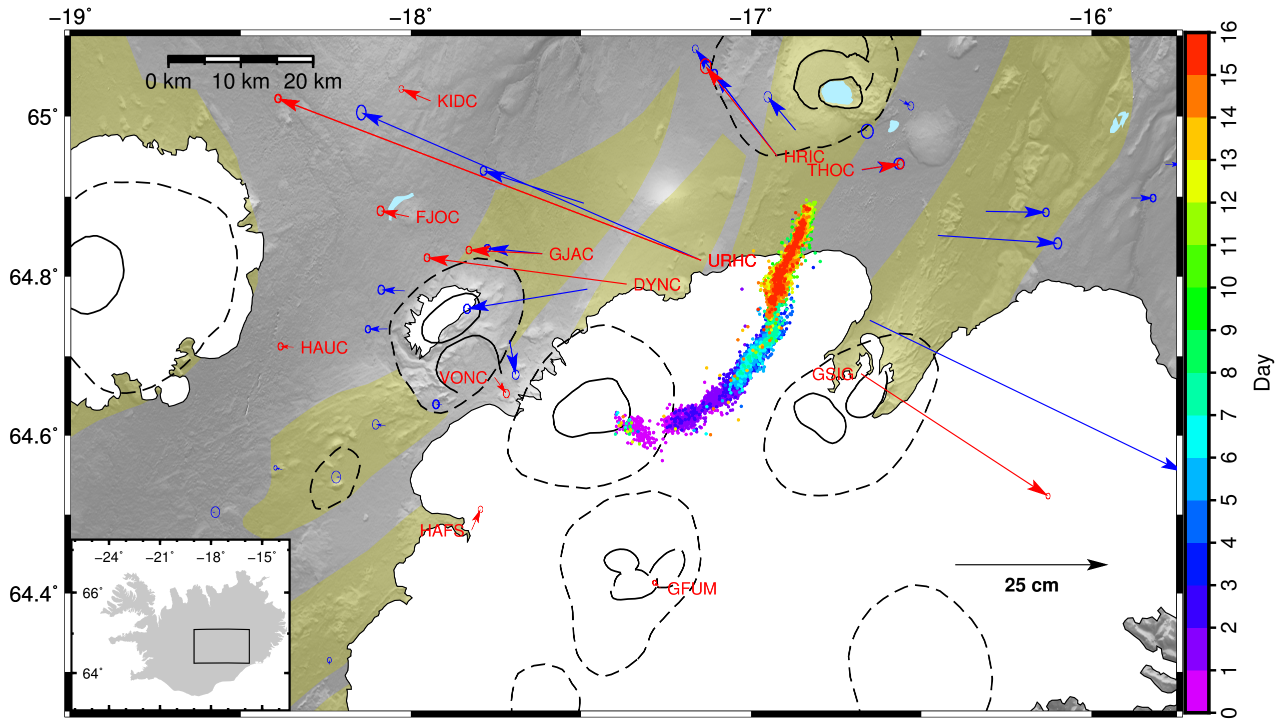

Figure 1. Geographic location of the Bárðarbunga volcano, dike seismicity and net GPS displacements. Dashed lines mark individual central volcanoes, solid lines are caldera faults and yellow shaded areas are fissure swarms associated with central volcanoes. Vectors show cumulative displacement spanning the duration of the diking event. Red arrows, and labels, are continuous GPS stations used in the time-dependent inversion. Blue arrows are campaign GPS stations. Dots show dike seismicity from *Ágústsdóttir et al.* [2019], which are color-coded by days since the beginning of the intrusion.

The initial analysis of seismicity [*Sigmundsson et al.*, 2015] revealed some variability in focal mechanisms among the larger events, ranging from strike-slip to normal; most estimated focal mechanisms were significantly oblique. A later study by *Ágústsdóttir et al.* [2016] investigated focal mechanisms at the distal end (the last ∼13 km) of the dike with a much denser network. They found the dominant focal mechanism (85 % of analyzed events) to be strike-slip with consistently the same strike and no significant volumetric component. Based on which nodal plane was better constrained by the data and stress field considerations, they concluded that these are left-lateral events with strike 38° East of North. The dike in this region strikes 25°. The other common focal mechanisms in this region are right-lateral slip with a strike of $\sim 17°$. That mechanism tends to occur only behind the leading edge of the dike. Analysis of other focal mechanisms show that along the first $0 - 10$ km of the dike the events are highly variable. From $10 - 30$ km, the mechanisms appear to have similar strike as the end region ($\sim 38°$), but are predominantly right-lateral. From 30 km to the end region the events are predominantly left lateral (see *Ágústsdóttir et al.* [2019] for details). We apply these inferred fault planes as prior constraints, as detailed in section 3.4.

Several studies modeled the surface deformation due to the dike and the caldera collapse associated with the Bárðarbunga rifting event [*Sigmundsson et al.*, 2015; *Green et al.*, 2015; *Ruch et al.*, 2016; *Parks et al.*, 2017]. However, most of the published studies have employed kinematic dislocation models. In contrast, in this study, we try to model realistic near field stresses. This is required to capture the temporally complex propagation of seismicity (Figure 1), and to accurately predict the cumulative number of earthquakes. As a result, our dike model has finer spatial and temporal discretization than previous studies, which is made possible by deriving the dike opening from traction boundary conditions, instead of treating the dike opening kinematically. In the following section, we describe the dike model in detail, along with a description of its limitations.

2 Methods

2.1 Dike model

Dike opening is controlled by the difference between the dike normal stress $\sigma = P_{litho} + \sigma_n$ and the magma pressure P; the dike overpressure is $\Delta P = P - \sigma = P - (P_{litho} + \sigma_n)$ (Figure 2a-b). Here, P_{litho} is the lithostatic pressure and σ_n is the component of the tectonic stress field that is normal to the dike. The density of the crust varies with depth, and at shallow levels is typically lower than the density of basaltic magma. The density constrast can stabilize the dike and promote lateral propagation [e.g. *Fialko and Rubin*, 1999; *Townsend et al.*, 2017]. The depth where the density of the magma and crust is the same is referred to as the level of neutral buoyancy (LNB). This may not be where the maximum opening occurs, since that also depends on σ_n.

At the top and bottom boundary of the dike the overpressure may change sign even though the dike opening is non-negative. Furthermore, at the propagating dike tip (Figure 2c) there is likely a (magma) lag region and a cavity filled with pore-fluids from the crust or exsolved volatiles from the magma [*Rubin*, 1993]. The pressure inside the cavity is highly uncertain, but one end member case is that the cavity pressure is negligible such that the overpressure is $\Delta P = -\sigma$, and is assumed here. The length of the lag can be solved for under the assumption that the crack is non-singular, as described later. A cavity also likely exists at the top and bottom margins (Figure 2b) but the depth dependence of $P-\sigma$ results in a more gradual transition where the over pressure becomes negative, resulting in a non-singular crack tip without introducing a magma lag (Figure 2a).

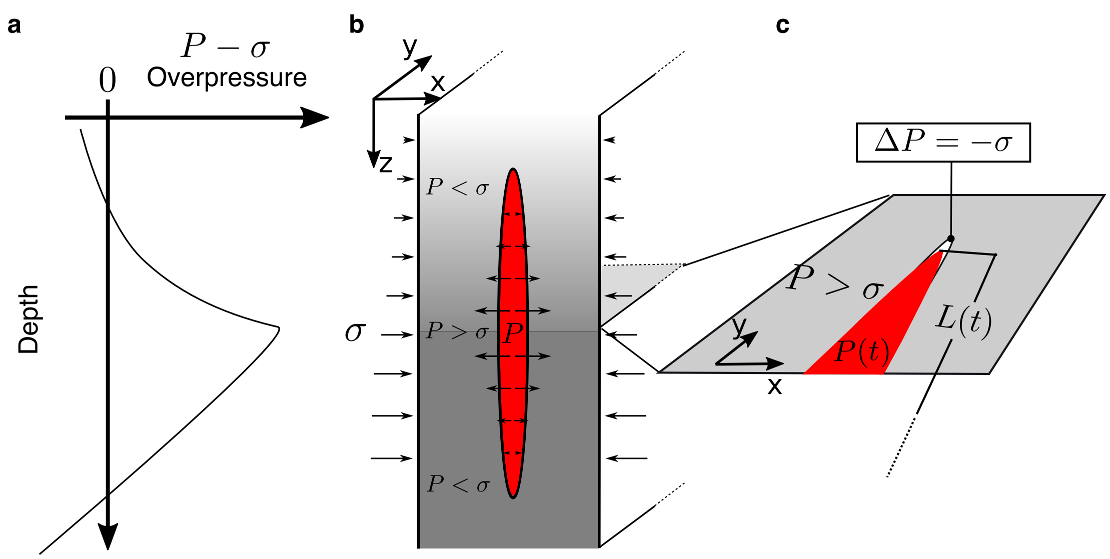

Figure 2. Schematic cross-section showing the depth dependent parameters that affect the dike. a, Schematic but generally characteristic overpressure profile within a vertical dike cross section. b, Schematic dike opening with both top and bottom tip under-pressured. c, Dike tip at the lateral end with a crack tip cavity and length $L(t)$ defined as the distance to the front of the pressurized magma. **Note the vertical section is elliptical which is not consistent with the overpressure profile**

To attain realistic stresses in the near field, we simulate a non-singular crack. It is fairly straightforward to compute the crack tip lag for a simple 1D geometry given a specified pressure distribution [e.g. *Fialko and Rubin*, 1999]. However, this is less obvious when the crack is 2D and pressure boundary conditions are non-uniform. We developed a method that achieves this for arbitrary under-pressure conditions or geometry.

The process is iterative and is loosely based on simulating the fracture process during an intrusion. One starts by setting up a grid of dislocation elements that cover areas of interest where magma may be located. The iterative approach can then be described in the following steps:

1. Select dislocations that are subject to positive overpressure, this is where the magma is guaranteed to be located. This represents the initial singular crack.
2. Use the boundary element approach (described below) to solve for dike opening.
3. Compute normal tractions on the rest of the grid due to dike opening and background stress.
4. Find elements subject to less compression than the predefined crack under-pressure at that location. If there are no such elements the stress singularity has been canceled to the resolution of the grid, otherwise continue to the next step.
5. Assign under-pressure to these elements and move to step 2.

The vertical distribution of overpressure is parameterized by a single value of magma pressure at the level of neutral buoyancy $P(z_{LNB})$, where the crustal density is the same as the magma density. The lateral extent of dike overpressure is indicated by a free parameter L that controls the dike length along strike. Crack opening beyond L is found by computing the size of the lag region such that the stress singularity is canceled. The dike overpressure $\Delta P(z)$ along a vertical cross-section is

$$\Delta P(z) = \rho_m g(z - z_{LNB}) + P(z_{LNB}) - \sigma(z), \quad (1)$$

where z is depth, ρ_m is magma density, $\sigma = \sigma^T_{ij}\nu_i\nu_j + P_{litho}(z)$ is the dike normal traction (ν_i is the dike plane normal vector and thus $\sigma_n = \sigma^T_{ij}\nu_i\nu_j$) due to the stress tensor σ^T_{ij} derived from tectonic loading and P_{litho}, the lithostatic pressure which is computed from the density of for the Icelandic crust from *Guðmundsson and Högnadóttir* [2007], based on data from *Carlson and Herrick* [1990] and *Christensen and Wilkens* [1982]. The tectonic stress is computed from a (tapered) buried opening dislocation to model deep rifting and plate spreading. The opening is tapered using a segment of a fourth order polynomial with zero slopes at both ends to attain non-singular stresses (see section 3.2.1 for details). The initial crack for the algorithm, described above, is taken as the region where $\Delta P > 0$ for all dislocations that are located within distance L along the length of the dike plane. Thus L does not represent the fracture length, which varies with depth, but the length where $\Delta P > 0$ at $z = z_{LNB}$.

2.2 BEM implementation

The surface in which the dike can propagate is fixed based on the seismicity and has fixed dislocation element discretization. This is a different approach than taken by *Segall et al.* [2013], where the dislocation discretization of the dike evolved as the dike propagated. The latter approach allows the length of the dike $L(t)$ to be a continuous variable. In contrast, the approach taken here renders $L(t)$ discrete, for computational efficiency admissible lengths are predefined by the initial discretization of the dike. This, in turn, results in an objective function that is a discrete function in the L dimension of the model space and is thus not differentiable; therefore, gradient-based optimization methods are precluded. In spite of these drawbacks, there are significant advantages in terms of computational efficiency since repeated calculations of the Green's functions are avoided.

Consider the matrix of influence coefficients $\boldsymbol{G}$ that relates a vector of opening $\boldsymbol{b}$ to the vector of over pressure acting on each dislocation element $\boldsymbol{\Delta P}$ in an elastic half-space:

$$\boldsymbol{\Delta P} = \boldsymbol{G}\boldsymbol{b} \Rightarrow \boldsymbol{b} = \boldsymbol{G}^{-1}\boldsymbol{\Delta P}. \tag{2}$$

Computing $\boldsymbol{G}$ is computationally expensive. For n opening mode dislocations, $\boldsymbol{G}$ has n^2 elements. If the crack geometry or discretization changes then all or a part of $\boldsymbol{G}$ changes, such that if BEM is used for a time-dependent inversion $\boldsymbol{G}$ typically changes in every iteration. That is how the dike model for the joint inversion by *Segall et al.* [2013] was constructed. However, since they assumed a planar dike, they could use translational symmetry to reduce the number of function calls. The 2014 Bárðarbunga dike is not planar, which means that such symmetries do not exist. We, therefore, compute $\boldsymbol{G}$ only once for a fixed grid and store the matrix. The algorithm outlined in Section 2.1 is then used to select dislocation elements that contribute to the opening of dike model. The rows and columns of $\boldsymbol{G}$, and elements of $\boldsymbol{\Delta P}$ that correspond to elements outside the periphery of the dike, including the tip cavity, are removed before the matrix is inverted to solve for the vector of opening $\boldsymbol{b}$.

2.3 Modeling the seismicity rate

Due to the kinked path of the Bárðarbunga dike, we cannot use the same approach as *Segall et al.* [2013] where the seismicity rate is computed in rectangular voxels. In order to best utilize the seismicity data, we form a mesh of tetrahedra elements surrounding the dike (Figure 3). The tetrahedral mesh is chosen such that voxels do not cross the dike plane. Dislocations have stress singularities that are proportional to the opening, or if dislocations align in the same plane, to the difference in opening of two adjacent dislocations. Thus, a smoothly varying opening will greatly decrease the influence of these singularities. However, if the voxels intersect the dike plane stresses may be evaluated too close to a dislocation edge producing un-realistic values. In our implementation, the stress tensor is evaluated at Gauss points in each tetrahedron; since Gaussian quadrature only makes use of points in the interior of the integration domain, this further limits the influence of singular stresses. An efficient way to implement the meshing and guarantee that voxels do not cross the dike plane is to use Delaunay triangulation. It has the property that nearest neighbors form an edge of the same triangle. Thus, by making sure any point on the dike plane also has the nearest neighbor on the dike plane, then the voxels will not intersect the plane of the dike (Figure 3).

Once a voxel system has been formed, and the points of the Gaussian quadrature in each voxel have been specified, the stress tensor can be evaluated at the Gauss-points and then projected into the normal and shear traction components, consistent with the observed focal mechanisms.

We compute the cumulative number of earthquakes N using the modified Dieterich 1994 theory of *Heimisson and Segall* [2018]:

$$\frac{N}{r} = \frac{A\sigma_0}{\dot{s}_b} \log\left(\frac{\dot{s}_b}{A\sigma_0}\int_0^t K(t')dt' + 1\right), \tag{3}$$

where r is the background rate of seismicity for a population, which we define for each voxel. A is a constitutive parameter related to the direct effect in the constitutive law and relates changes in slip rate to friction. τ_0 and σ_0 are the initial shear and normal stresses acting on the fault and $\dot{s}_b$ is the background Coulomb stressing rate where the coefficient of friction is $\mu = \tau_0/\sigma_0 - \alpha$. Here, α is a constant related instantaneous changes in state due to variations in normal stress [*Linker and Dieterich*, 1992]. The characteristic decay time of seismicity is given by $t_a = A\sigma_0/\dot{s}_b$. Time dependent stress changes due to the intrusion are accounted for in the kernel $K(t)$:

$$K(t) = \exp\left(\frac{\tau(t)}{A\sigma(t)} - \frac{\tau_0}{A\sigma_0}\right)\left(\frac{\sigma(t)}{\sigma_0}\right)^{\alpha/A}, \tag{4}$$

where $\tau(t)$ and $\sigma(t)$ are the total shear and effective normal stress respectively.

We apply the trapezoidal rule to the integral (3) in each voxel and numerically estimate the scaled cumulative number of earthquakes $\tilde{N} = N/r$ at time t_i (where $t_1 = 0$). In the m-th Gauss point in the n-th voxel the following approximation of Equation (3) for the cumulative number of events is attained:

$$\tilde{N}^{n,m}(t_i) = \frac{A^n {\sigma_0}^{n,m}}{{\dot{s}_b}^{n,m}} \log\left(\frac{{\dot{s}_b}^{n,m}}{A^n {\sigma_0}^{n,m}} \sum_{j=1}^{j=i} \frac{1}{2}(K^{n,m}(t_j) + K^{n,m}(t_{j+1}))(t_{j+1} - t_j) + 1\right), \tag{5}$$

where ${\dot{s}_b}^{n,m} = {\dot{\tau}_b}^{n,m} - ({\tau_0}^{n,m}/{\sigma_0}^{n,m} - \alpha^n){\dot{\sigma}_b}^{n,m}$ is the background Coulomb stressing rate at Gauss point m in voxel n. The kernel can be written in the same notation

$$K^{n,m}(t_j) = \exp\left(\frac{\tau^{n,m}(t_j)}{A^n\sigma^{n,m}(t_j)} - \frac{\tau^{n,m}(t_1)}{A^n\sigma^{n,m}(t_1)}\right)\left(\frac{\sigma(t)^{n,m}}{\sigma(t_1)^{n,m}}\right)^{\alpha^n/A^n}. \tag{6}$$

For further discussion on the meaning of various parameters and the derivation of equations (3) and (4) we refer the reader to *Heimisson and Segall* [2018].

We estimate the total number of predicted events in the n-th voxel N^n based on the scaled number events at the m Gauss points:

$$N^n(t_i) = r^n \frac{\sum_m w_{(n,m)} \tilde{N}^{(n,m)}(t_i)}{\sum_m w_{(n,m)}}, \tag{7}$$

where $w_{(n,m)}$ are the Gauss weight of point m in voxel n and r^n is the background rate of seismicity per unit volume of the n-th voxel.

Equation 4 depends on the absolute shear and normal stress acting on a fault plane. The initial shear stress τ_0 is the component of the traction vector for a given fault orientation parallel to the slip vector and computed directly from the dislocation model of the plate boundary, discussed in section 3.2.1, and $\Delta\tau(t)$ is the stress change due to dike opening. These two form the total shear stress: $\tau(t) = \tau_0 + \Delta\tau(t)$.

The effective normal stress acting of a population of seismic sources $\sigma(t)$ is a combination of several factors,

$$\sigma(t) = \sigma_0 + \Delta\sigma(t), \text{ where } \sigma_0 = P_{litho} - \rho_w g z + \sigma_n \tag{8}$$

where P_{litho} is the lithostatic pressure estimated from the density structure in Iceland [*Guðmundsson and Högnadóttir*, 2007] , $\rho_w = 1000$ kg/m^3 is the density of water and z the depth below the Earth's surface. σ_n is the normal component of the traction acting on the fault plane dislocation model of the plate boundary and $\Delta\sigma(t)$ is the time-dependent normal stress induced by the dike opening.

3 Inversion

The dike opening model developed in section 2.1 is a function of the imposed tectonic stress field, the lithostatic pressure gradient, the excess magma pressure and the magma density itself. All these fields influence the traction boundary conditions on the dike surface. We constrain parameters that control these fields with deformation data (Section 3.2). Since these do not change with time (except the excess magma pressure) we use InSAR and GPS data spanning the full intrusion [data from *Sigmundsson et al.*, 2015]. to estimate the time-independent fields. Next we estimate the time-depend fields (length and pressure history of dike) using the GPS time series data. Finally, frictional and seismicity rate parameters are estimated from a temporal inversion of the number of earthquakes (Section 3.4). In each subsequent step, the results of the previous inversion are used as constraints so that self-consistency is maintained.

3.1 Treatment of observations

To determine the cumulative number of events, we first assign each earthquake to a voxel. We use the catalogue of *Ágústsdóttir et al.* [2019] and magnitude estimates from *Greenfield et al.* [2018] and filter the catalogue for our estimated magnitude of completeness of $M_c = 1$. If an event is not inside any voxel (about 2% of events) it is not included. The total time history $N(t)$ is interpolated using a piecewise cubic Hermite interpolating polynomial; then the interpolant is evaluated at predefined time steps. This method of interpolating is chosen because it is shape preserving and has a continuous first derivative. The shape preserving property means that the derivative is non-negative,

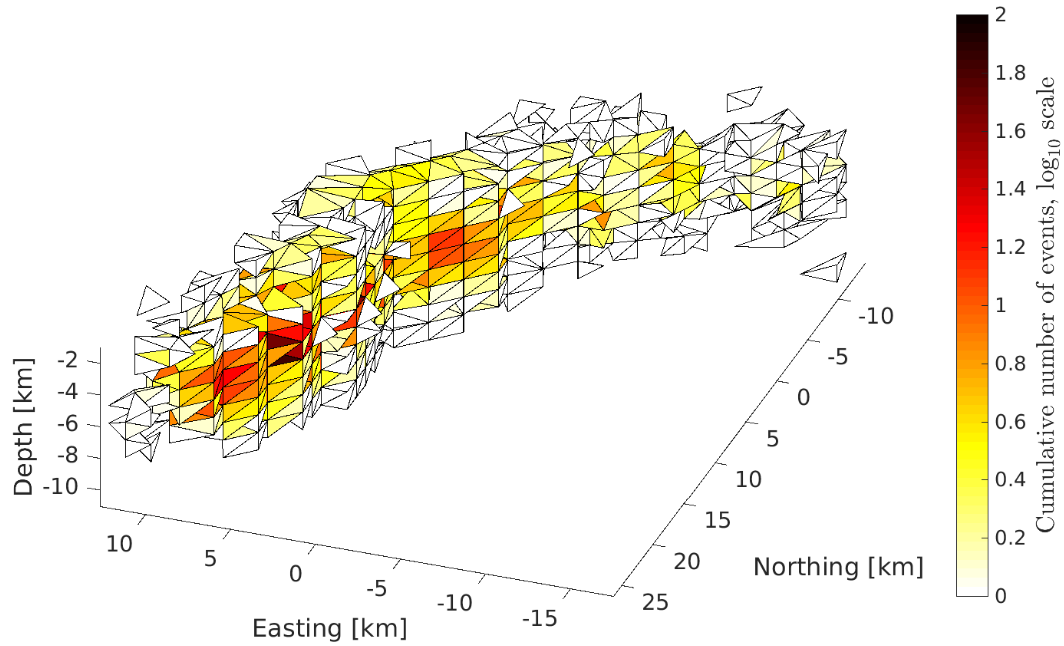

Figure 3. Total number of earthquakes in each voxel, binned into a mesh of voxels with mean edge length of 1.5 km.

which is required as a negative seismicity rate is not physical. To account for errors in earthquake hypocenters the locations of events are randomly perturbed within the estimated error bounds from *Ágústsdóttir et al.* [2019]. The events are thus assigned multiple times to voxels; and the mean value of earthquakes at each time step is taken to be $N_{obs}(t)$ and the standard deviation is $\sigma_{eq}(t)$.

We estimate that 100 timesteps over a period of 16 days (during which the dike propagated and subsequently erupted) are needed in order to resolve first order time-dependent features in the seismicity. In order to determine the cumulative GPS displacements at these 100 time steps we interpolate the 8h time series (Figure 4) using a piecewise linear interpolation. The interpolation corresponds to upsampling the GPS time series by approximately a factor of two.

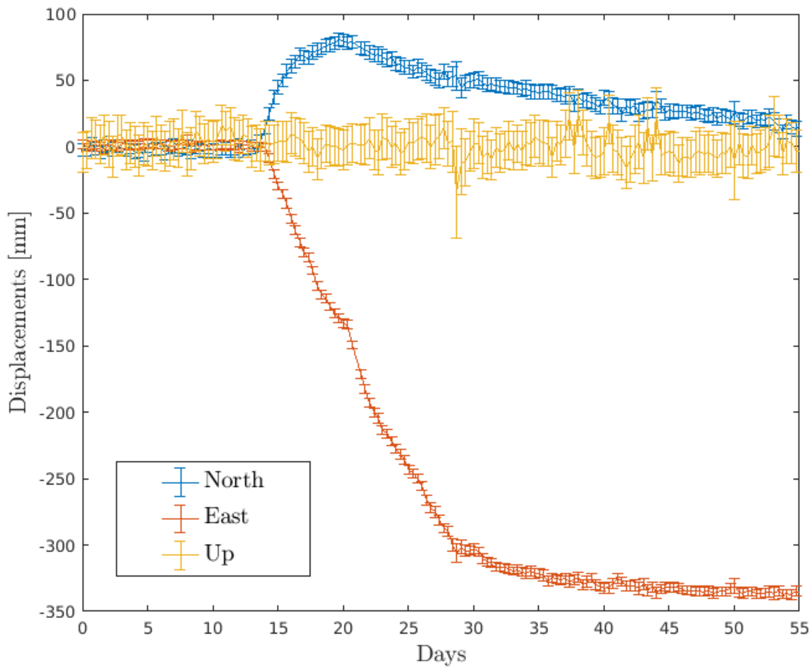

Figure 4. 8 hour time-series at station DYNC. Dike starts propagating at around day 15. Location of DYNC is shown in Figure 1.

3.2 Constraining the background stress field

3.2.1 Model setup

Plate boundary deformation in the rift-zones of Iceland has previously been modeled using a simple buried dislocations [*LaFemina et al.*, 2005; *Árnadóttir et al.*, 2006]. This model assumes a constant rate of plate spreading below the brittle-ductile boundary under the central axis of the rift. This is represented as an infinitely deep vertical opening dislocation. The buried dislocation model is a highly idealized, yet has been shown to satisfy surface deformation data reasonably well in multiple tectonic settings, since first applied to a transform plane boundary by *Savage and Burford* [1973]. It is thus a reasonable first-order model to capture tectonic stresses that may have build up between diking events.

Due to the stress singularity at the edge of the buried dislocation model, we taper the opening constrained such that the opening gradient goes to zero at the topmost edge l_u, while at depth l_b the opening reaches the full far-field extension rate. Thus, l_b correspond crudely to the brittle-ductile boundary, where very little stress from tectonic loading remains (Figure 5). This results in nonsingular stresses at l_b and l_u.

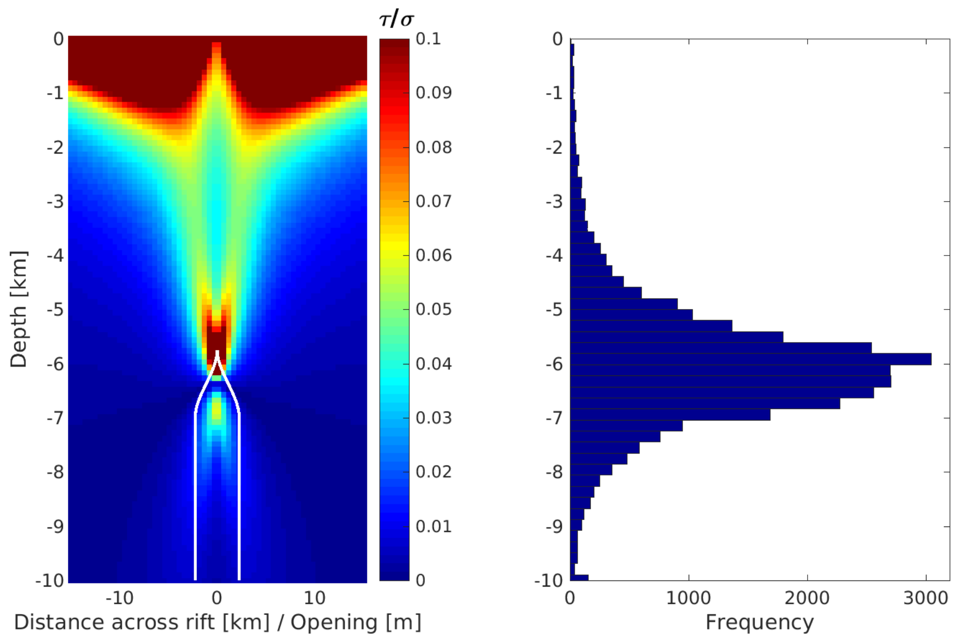

Figure 5. Depth dependent stress field predicted by a tapered buried dislocation. Left: Ratio of horizontal shear stress to normal stress assuming lithostatic minus hydrostatic pressure gradient of $g{\cdot}1750$ kg/m^3 with depth, with shear stress computed on a plane striking 15° east of the rift axis. Modified buried dislocation opening is shown with white lines with $l_b = 7$ km, cumulative opening of 4.5 m and tapers to 0 at $l_u = 5.75$ km depth. Right: Histogram of earthquakes with depth located by *Ágústsdóttir et al.* [2016]. High ratios of τ/σ promote higher rates of seismicity.

In 1797 a dike propagated from Bárðarbunga and erupted in the Holuhraun area, the 2014 Bárðarbunga dike reoccupied the same crater-row produced by the 1797 dike and eruption [*Hartley and Thordarson*, 2013; *Sigmundsson et al.*, 2015]. It is expected over the time-span of 217 years that the cumulative opening deficit within the shallow rift zone due to plate motion is $\sim$ 4 m, given an extension-rate of 17.4 mm/yr [*Drouin et al.*, 2017]. Extension over the graben formed by the 2014 Bárðarbunga dike was in fact around 4.5 m [*Ruch et al.*, 2016]. It is, therefore, natural to constrain the opening of the buried dislocation to be in the range 4.0 – 5.0 m. The rift axis strikes $\sim 13.30° - 15.85°$ [*Heimisson et al.*, 2015a], with its center under the Askja volcanic system north of the

2014 eruption [*Sturkell and Sigmundsson*, 2000]. The depth to the brittle-ductile boundary has been estimated to be between 6 to 8 km [*Soosalu et al.*, 2010; *Key et al.*, 2011], based on the depths of earthquakes. However, from fitting a buried dislocation to the plate boundary deformation in the Eastern Volcanic Zone in Iceland, *LaFemina et al.* [2005] found a best fitting depth of 13 km, although elastic dislocation models ignore possible viscoelastic effects which may bias the depth. Most earthquakes during the 2014 dike intrusion were between 6 – 8 km depth, which suggests that 8 km is a lower limit to a range from 8 to 13 km depth for l_b. We keep the difference $l_b - l_u = 0.5$ km, constant in the inversion described later.

The density structure plays an important role in determining the lithostatic stress. Here, we use estimates from *Guðmundsson and Högnadóttir* [2007] and consider the density to increase linearly to depth d_t of 4 – 6 km. Below d_t the density is considered constant. We parameterize this density profile through two parameters: $\rho_1 = 2200 - 2400$ kg/m^3 (shallow crust), $\rho_2 = 2850 - 3000$ kg/m^3 (density at d_t and below). Typical laboratory measurements of liquid basalt exhibit a range of densities of 2650 – 2800 kg/m^3 [*Sparks et al.*, 1980]. To reflect uncertainty for magma *in situ*, we allow a slightly larger range of 2600 – 2850 kg/m^3, so that magma is negatively buoyant in the upper crust.

To summarize, we compute the stress before the diking event as a superposition of a tectonic stress field, derived from a tapered buried dislocation and a density structure that gives rise to a lithostatic pressure. The buried dislocation model is governed by the following parameters: The depth to the top of the dislocation l_b, its strike and location of the axis (±2.5 km with respect to Askja caldera center [*Heimisson et al.*, 2015a]). The lithostatic pressure depends on the two densities ρ_1 and ρ_2 and the transition depth d_t.

3.2.2 Inversion procedure

The previous section described ranges of parameters that factor into the tectonic and lithostatic stress field. Here we show how these ranges are narrowed to preferred estimates using InSAR and GPS data. We select 11 interferograms that have been processed and down sampled by *Sigmundsson et al.* [2015] and GPS displacements from 12 stations (Figure 1) that span the entire duration of the dike intrusion. The dike model

Table 1. Summary of parameters and estimated ranges for the stress model

Symbol	Description	Range	Optimal value
Density structure			
d_t	Depth of density gradient changes	4 – 6 km	4.3 km
ρ_1	Near surface density of the crust	2200 – 2400 kg/m^3	2350 kg/m^3
ρ_2	Density at depth d_t	2850 – 3000 kg/m^3	2900 kg/m^3
ρ_m	Magma density	2600 – 2850kg/m^3	2610 kg/m^3
Buried dislocation			
Strike	Strike (degrees East of North) for rift axis	13.30 – 15.85°	13.30°
l_b	Dislocation locking depth	8 – 13 km	8.0 km
Opening	Net cumulative opening	4 – 5 m	5.0 m
Easting	Uncertainty in Easting location of axis at fixed latitude	±2.5 km	1.36 km

is used to predict net GPS displacements and line of sight displacement for the 11 interferograms. We minimize a L_2 objective function

$$\chi^2 = (\boldsymbol{d} - \boldsymbol{G}(\boldsymbol{m}))^T \boldsymbol{\Sigma_d}^{-1} (\boldsymbol{d} - \boldsymbol{G}(\boldsymbol{m})), \tag{9}$$

where $\boldsymbol{G}$ represents the forward operator that maps a model vector $\boldsymbol{m}$ to line of sight surface displacement and east, north, and up GPS components. The corresponding data are contained in vector $\boldsymbol{d}$. The variance-covariance matrix, $\boldsymbol{\Sigma_d}$, follows *Sigmundsson et al.* [2015] in estimating the spatial covariance of the InSAR data; the GPS error is assumed to be spatially uncorrelated.

To compute predicted displacements, three parameters are required in addition to those listed in Table 1: ΔV, the volume change of a Mogi source representing caldera deflation at fixed location [from *Parks et al.*, 2017], $P(z_{LNB})$ from equation 1 and L the dike length. The timespan of the interferograms varies considerably with the later acquisition time ranging from August 26 to September 20, 2014. The length of the dike likely did not change after August 26 [*Sigmundsson et al.*, 2015; *Spaans and Hooper*], although, the dike pressure and the chamber volume were still evolving. ΔV is inherently time-dependent, but is included as a constant to approximately correct for the far field displacement from the magma chamber pressure drop, it does not accurately capture the complicated near field deformation which was a combination of a caldera collapse and a deeper depressurization [*Parks et al.*, 2017]. More importantly $P(z_{LNB})$ changed with time and in the next section will be estimated as such, however, in this step of the inversion the goal is to estimate the time-independent parameters and we thus take $P(z_{LNB})$ as constant between 8/26 – 9/20. Approximating ΔV and $P(z_{LNB})$ as constants in this time interval results in additional misfit between model predictions and data. However, allowing a different value of ΔV and $P(z_{LNB})$ for every interferogram resulted in a model space that was too large to converge confidently. For this step in the inversion, we regard ΔV, $P(z_{LNB})$, and L as nuisance parameters and their estimated values are not utilized in later steps of the inversion procedure.

3.2.3 Results: Crustal Model

The inversion procedure starts by finding a good fit to the data using a genetic algorithm [*Goldberg and Holland*, 1988]; it then attempts to improve the fit further using a direct search algorithm [*Audet and Dennis Jr*, 2002]. Both steps enforce uniform priors on the parameter values (Table 1). Running this scheme repeatedly we find that it consistently converges to the same minimum, which we interpret as the global minimum. The optimal values for the crustal model are reported in Table 1. These maximum likelihood values are used in the following, time-dependent part of the inversion.

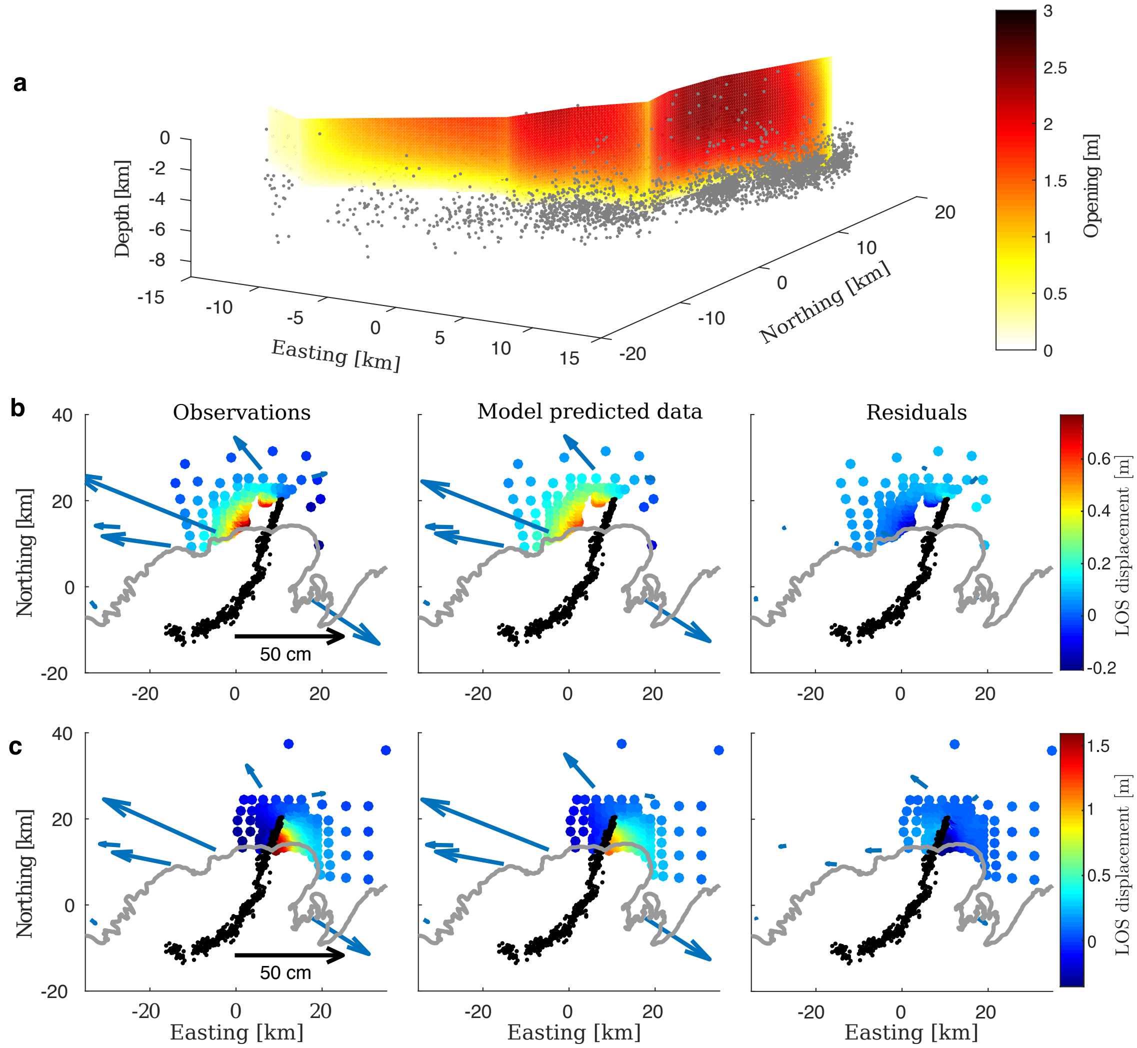

Figure 6. The static dike model (a) and comparison of the observations, model predicted data and residuals for TerraSAR-X (26 July 2012 – 4 Sept. 2014, ascending) (b) and Cosmo-SkyMed (August 13–29 2014, descending) interferograms (c). Arrows indicate horizontal GPS displacements at the time of the final InSAR acquisition. The bottom edge of the model dike is roughly coincident with the seismicity.

Figure 6 shows the opening distribution of the static dike model and two examples of interferograms that are used in the inversion. The static dike model shows that its lower tapered edge agrees well with the depth of earthquakes. This agreement is not enforced and the model space does allow for dike models that would extend substantially deeper or shallower. The deformation residuals suggest good agreement, although significant residuals are expected due to treating ΔV and $P(z_{LNB})$ as time-independent as discussed in the previous section.

3.3 Time-dependent estimation of dike pressure and stressing history

In this section, we estimate the dike overpressure and stressing history in each voxel as functions of time during the intrusion. In the previous section, the time-independent parameters that determine the stress field were estimated (Section 3.2.1). These are used to set the initial conditions of the stresses and background stressing rates (equations 3 and 4). The time-dependent stress ($\Delta\tau(t)$ and $\Delta\sigma(t)$) field is derived from the temporal evolution of the dike. In this section, we show how the stressing history at the Gauss points in each voxel are determined, which is required to compute the predicted seismicity.

The 8 hour GPS time series is interpolated into 100 time steps, corresponding roughly to 1 point per 4 hours. This upsampling was necessary to resolve characteristics of the seismicity that occur on time scales shorter than 8 hours. For each time step the length of the dike $L(t)$ is determined by the advancing swarm of seismicity; the magma is assumed to be 1 km behind the location of the highest seismicity rate during that time step. $L(t)$ is assumed not to change if the point of highest seismicity rate retreated relative to the previous position. Thus, the dike can only lengthen or stay constant. At each time step the magma pressure at the level of neutral buoyancy $P(z_{LNB}, t)$ is optimized by fitting the GPS data. An objective of the same form as equation 9 is minimized where the variance-covariance $\boldsymbol{\Sigma_d}$ is diagonal. At the beginning of each time step, we find the least squares solution for the volume change of a Mogi source, representing the deflating magma reservoir. Two stations VONC and HAUC (Figure 1) are used to constrain this volume change since they are close to the caldera and show limited sensitivity to the dike. The predicted displacements from the Mogi source are used to correct the GPS time series at other stations before the time-dependent dike inversion is performed. We apply this correction instead of inverting for $P(z_{LNB}, t)$ and volume change of the Mogi source simultaneously due to the computational requirements needed to converge an objective with a time-varying 2D model space. Furthermore, the deflation signal in the far field is much less than the dike signal. Note that the dike geometry (i.e., which dislocations open) depends on the pressure $P(z_{LNB}, t)$, this is, therefore, not a linear inversion.

From this inversion we obtain $L(t)$ and $P(z_{LNB}, t)$. This, along with the time-independent parameters constrained from InSAR is sufficient to derive an opening distribution for the dike at each time step. Using elastic Green's functions we compute the full stress tensor at the Gauss point in each voxel. The time history of the stress tensor at each Gauss point is used in the next step where the predicted number of events is compared to observations. Due to the sensitivity of the earthquake production to changes in stress, it is not sufficient to represent the stressing history in only 100 time steps. We thus assume that between time steps the dike advances at a constant velocity and the stress is evaluated at each Gauss point as it advances (every 200 m). The procedure results in a stressing history of about 1000 time steps. We found that the results are not sensitive to downsampling the stressing history by 50%, which implies convergence of equation 6. Several tests were made to check error associated with the integration of N in the voxels (equation 7), this included changing the dislocation size of the dike and varying the number of Gauss points and voxel size. We found that the current scheme using dislocation with an edge length of 200 m, voxels with a characteristic length of 1500 m and 3 point Gaussian quadrature (27 points in each voxel), resulted in a numerical error much smaller than the data error.

3.3.1 Results

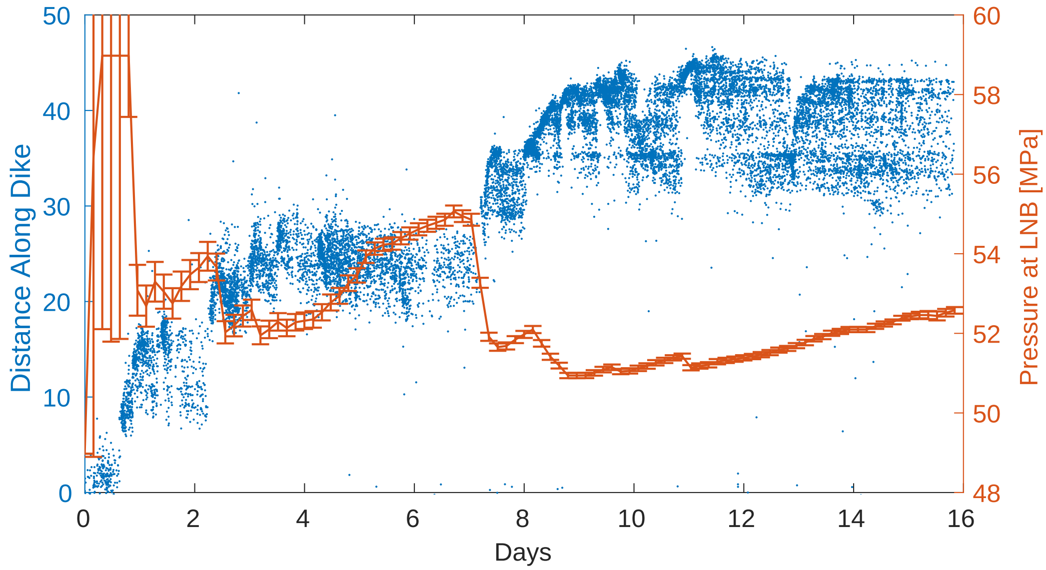

Figure 7. Comparison of the inferred time-dependent pressure and the space-time evolution of the seismic swarm. This reveals that as the dike advances the pressure drops and when arrested the pressure builds up again. Note that initially the signal-to-noise ratio is low. The initial large pressure values are not be well constrained as shown by the errorbars that provide an estimate of one standard deviation error of the pressure.

Results for $P(z_{LNB}, t)$ are shown in Figure 7, with an estimate of uncertainty that is derived by fixing the crack geometry to the optimal value found using the non-linear inversion scheme in Section 3.3. With fixed crack geometry, the inverse problem becomes linear, and the error propagation from the GPS error to the pressure estimate is straightforward. The error estimate reveals that initially the pressure value is highly uncertain.

The time-dependent inversion shows that the dike pressure increased during pauses in dike advance and dropped once rapid propagation recommenced, consistent with the interpretation of *Sigmundsson et al.* [2015]. During the pauses in propagation inflow of additional magma continues, which results in elevated pressure. However, when the dike advances, the potential dike volume increases, causing the pressure to decrease. These physical processes are not explicitly prescribed by the dike model but are required in order to fit the GPS data.

3.4 Inversion in voxels for seismic source and frictional properties

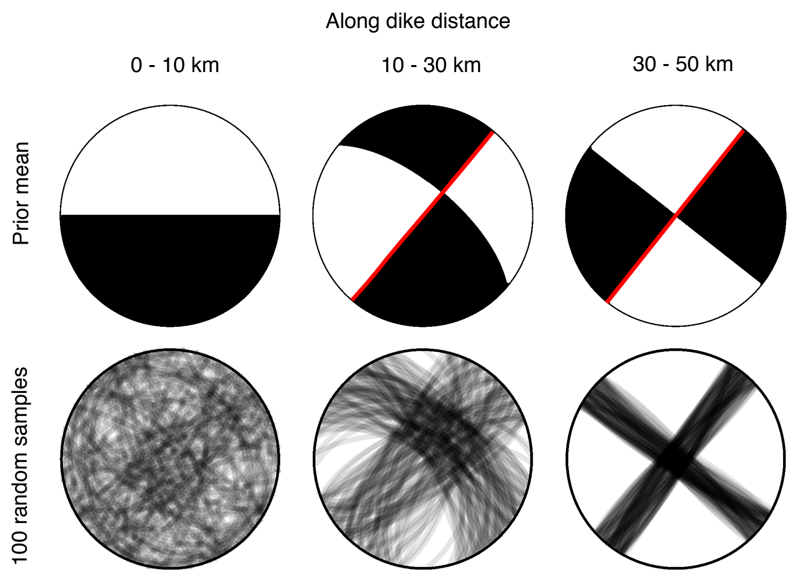

Figure 8. Visualization of the priors on focal mechanisms. Top row shows the resulting focal mechanism from the mean of the strike, dip and rake priors. Red line indicates the assumed fault plane. Bottom row shows 100 random samples from the prior distributions. Columns correspond to distance along dike length: the mechanism is uncertain for range 0 – 10 km, reasonably well constrained for 10 – 30 km and tightly constrained for $>$ 30 km [*Ágústsdóttir et al.*, 2019].

In the previous two steps, we constrained the background stress field and the time-dependent dike induced stresses based on geodetic and seismic data. In this section, we use those estimates to predict the cumulative number of earthquakes in each voxel (N in equation 3). Although many fields and parameter have been constrained in the previous steps there are still 6 additional parameters that relate to N, three characterizing the receiver fault orientation: strike, dip and rake, and three related to frictional properties and background stressing rate: A, α and r. We use a Markov Chain Monte Carlo (MCMC) approach to estimate posterior probability density functions for fault orientation (strike, dip, and rake) and earthquake productivity parameters (A, r, and α). All prior distributions are taken to be uniform with hard bounds which are described below.

We estimate strike, dip, and rake based on focal mechanisms and inferred fault planes from *Ágústsdóttir et al.* [2019]. For the first 10 km of the dike, a voxel can have essentially any fault orientation that could be considered reasonable for a rift setting (Figure 8), this is done to reflect the highly variable and uncertain focal mechanisms in this area. We allow either strike slip (both left and right lateral), normal or oblique (between strike slip and normal) with the dip constrained to be between $60-90°$. For the distance range of $10-30$ km the focal mechanisms exhibit right lateral strike slip with a strike of about $\sim 40°$. However, we allow for uncertainty in dip, strike, and rake (Figure 8) to reflect the focal mechanism variability. For the final 30 km, the focal mechanisms are tightly constrained, which translates into low variance in prior distributions (Figure 8).

The prior for the constitutive frictional parameter A is set to a wide range $10^{-5}-$ -0.02. Where the upper limit represents the highest values from experiments under hydrothermal conditions [*Blanpied et al.*, 1991], but the lower limit is estimated from the low values of $A\sigma_0$ that are commonly inferred when the *Dieterich* [1994] theory has been applied to field data [*Hainzl et al.*, 2010]. The background seismicity rate prior ranges from $2{\cdot}10^{-2}-10^{-5}$ events per year for a voxel of average size. The model includes $\sim$ 500 voxels, which means that at the upper bound we would expect on the order of 10 events per year. Prior to the diking event, no seismicity had been detected on large parts of the eventual dike path [*Ágústsdóttir et al.*, 2019]. We estimated the magnitude of completeness for the dike-induced events to be $\mathrm{M}_c = 1$, which is lower than that for the national seismic network. Small background events may, therefore, not have been detected. Nevertheless, it is likely that 10 events per year would have resulted in some large enough to be detected over the 23 years of automatic seismic monitoring prior to the 2014 Bárðarbung intrusion. However, the population of seismic sources (see *Heimisson* [2019] for precise definition) may not have been sufficiently stressed prior to the intrusion to produce earthquakes at a constant rate, in which case the background rate could not be determined prior to the diking event [*Heimisson and Segall*, 2018] (see section 4.1 for further discussion) and could be much higher than what can be inferred from observations. In this context, the background rate is the steady state seismicity rate that would eventually occur if the populations of seismic sources were subject to constant background stressing rate. We thus conclude that a broad *a priori* range is needed to reflect this uncertainty. The parameter α is related to instantaneous changes in the frictional state due to changes in normal stress [*Linker and Dieterich*, 1992]. We set α to a range of $0-0.5$.

We reject models where τ_0, μ, $\dot{\tau}_b$ or $\dot{s}_b$ are negative, which enforces additional constrains locally on the focal mechanism that are not reflected in Figure 8 and guarantee that only fault orientations are considered that are subject to stress conditions favorable for slip.

Sampling of the PDFs is done using an ensemble sampler algorithm proposed by *Goodman and Weare* [2010] (using the implementation of *Foreman-Mackey et al.* [2013]). The algorithm samples the log posterior distribution for each voxel:

$$\log(p(\boldsymbol{m}, \boldsymbol{\sigma}|\boldsymbol{d})) = -\frac{1}{2}\sum_i \left(\frac{d_i - G(\boldsymbol{m})}{\sigma_i}\right)^2 - \sum_i \log\left(\sqrt{2\pi}\sigma_i\right) + \log(p(\boldsymbol{m})), \qquad (10)$$

where d_i is the cumulative number of seismic events at the i-th timestep and σ_i is the corresponding standard deviation. G represents that forward operator that takes in the previously constrained stress fields and the six aforementioned model parameters, $\boldsymbol{m}$, and predicts the cumulative number of events in each voxel from Equation 5. Finally $p(\boldsymbol{m})$ is the prior probability distribution of the model parameters.

3.4.1 Results: voxel inversion

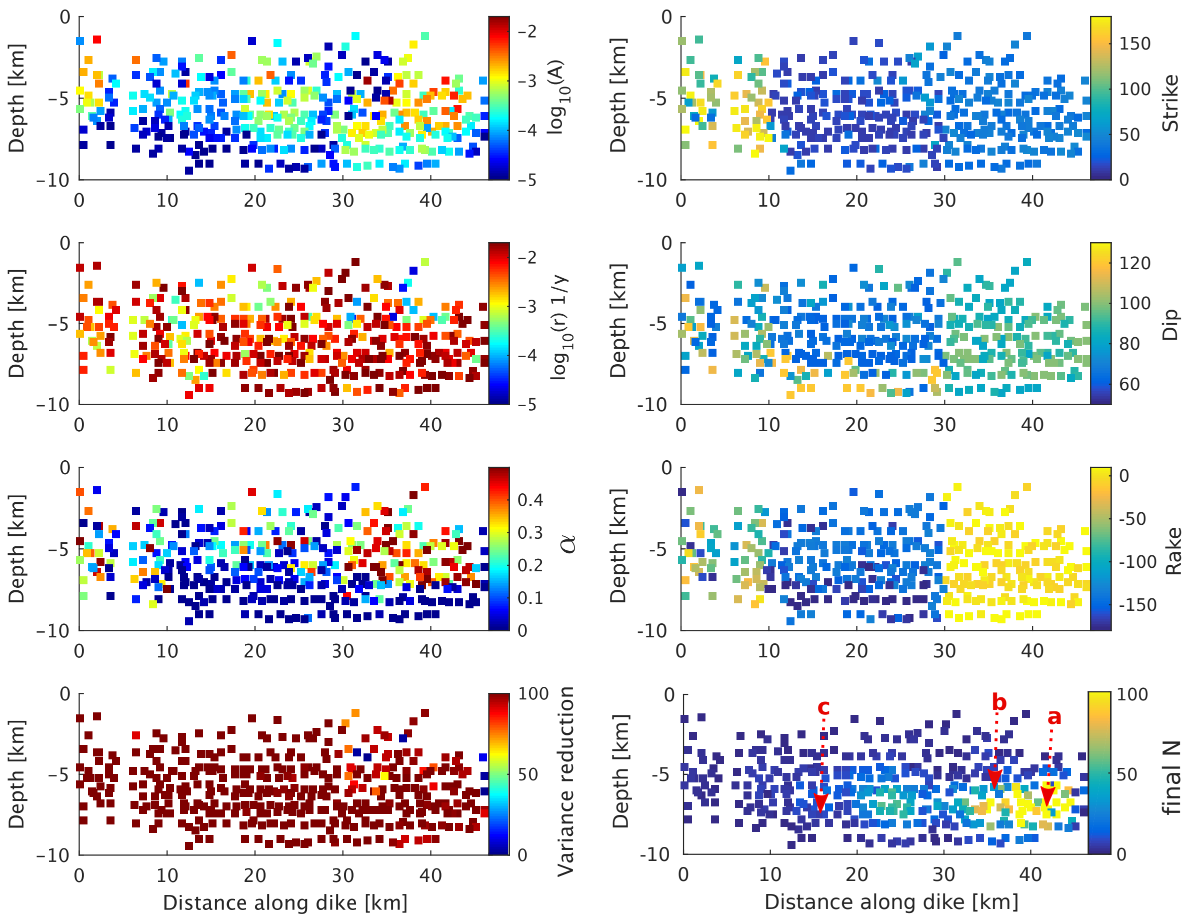

Figure 9. Maximum a Posteriori (MAP) values for model parameters estimated in each voxel, along with variance reduction and final cumulative number of events in the bottom row where labels **a**, **b** and **c** and corresponding arrows indicate the locations of voxels shown in Figure 10. Each square represents the center of a voxel projected in a depth versus distance-along-dike coordinates.

Inversion results (Figure 9) exhibit high spatial variability in many parameters of interest. The MAP (maximum a posteriori) estimate of A ranges from typical laboratory values ($A \sim 0.01$) to much smaller values ($A \sim 10^{-5}$) that are common in studies that apply the *Dieterich* [1994] model to seismic data, as discussed in Section 3.4. The parameter estimates show spatial correlation, although no such correlation or smoothing is prescribed in the inversion. This may suggest robustness in the inversion, although, if some of the assumptions are significantly and systematically incorrect, this may bias the parameter estimates. One such bias may stem from the assumptions on the dike tip underpressure, which was taken as an end member where the tip has a negligible fluid pressure ($\Delta P = -\sigma$). If additional fluid pressure is present ($\Delta P = P_f - \sigma$), then the near field stress perturbations are lower and distributed differently, which may systematically bias A. However, most of the earthquakes are not triggered at the dike tip but at the bottom of the dike where the opening tapers due to a vertical gradient in overpressure (Figure 6a). Thus the influence of the leading dike tip on the temporal evolution of the earthquakes may be diminished.

In the supplementary materials, we show the median value for each distribution, as well as 5% and 95% percentile values (Figures S1, S2, and S3). Figure 9 demonstrates that in the vast majority of voxels, the model can explain most of the a posteriori variance. Figure 10 shows the probability distributions for three different voxels, which all vary substantially in temporal behavior and the final cumulative number of events. One striking result in Figure 10 is how much influence the cumulative number of events has on the width of the distributions. There tends to be a very narrow range of model parameters that can fit voxels with more than 100 events, whereas having only a handful of events leads to broader distributions (see also Supplementary Figures S2 and S3). This further suggests that attempting to improve spatial resolution using smaller voxels will result in an increased variance of the model parameters.

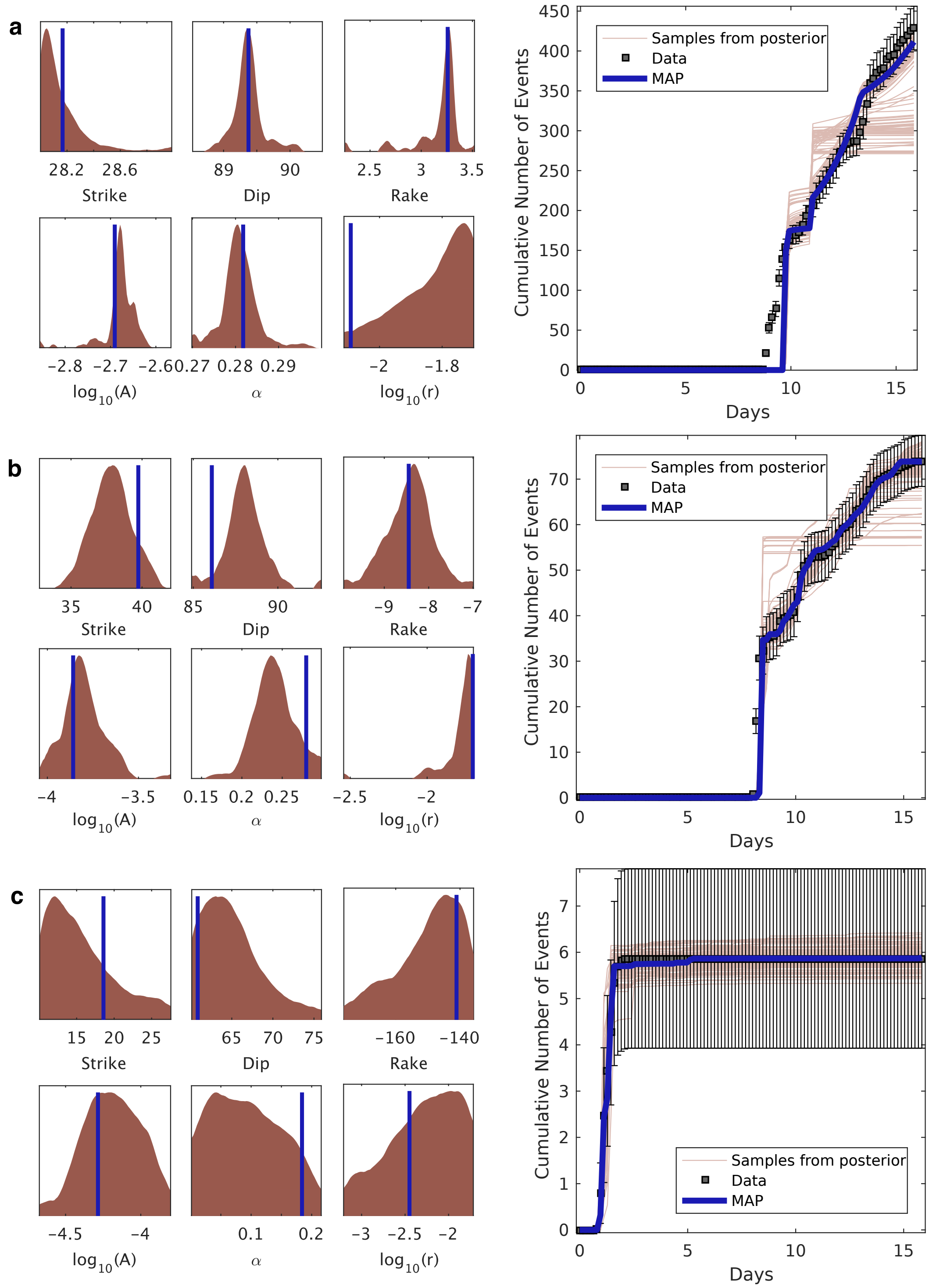

Figure 10. Parameter distributions (left) and predicted and cumulative number of events for three voxels (locations shown in Figure 9, bottom - right), vertical bar marks the MAP value and distributions are shown over their 95% confidence intervals. Voxels shown are picked to illustrate a wide range of total cumulative number of events with panel **a** showing the voxel with maximum number of events. The range of acceptable models strongly depends on the cumulative number of events.

The fit to the cumulative number of events curves is generally good (Figures 9 and 10). However, to investigate if the model resolves important space-time characteristics of the seismicity induced by the Bárðarbung dike, we generate a synthetic catalog. To do so, we round each predicted $N(t)$ time-series from the MAP to the nearest integer, rendering time-discrete events. Then, we assign time to each event by sampling from a uniform distribution with bounds at the previous and subsequent time steps. This procedure reveals that many of the important characteristics of the seismicity are produced by the model (Figure 11). Most importantly, the model predicts that actively intruding segments remain seismically active while all previous segments become more or less aseismic. For each voxel, we generally match the absolute number of events quite well, as reflected in the variance reduction (Figure 9). For computational reasons, we only run the inversion for about half the voxels and, therefore, do not match the absolute number of events in the catalog. However, the voxels selected for the MCMC sampling are picked to represent, in an unbiased manner, all seismically active regions surrounding the dike. For a 3D view of the dike model and simulated seismicity see the supplementary movie (Movie S1).

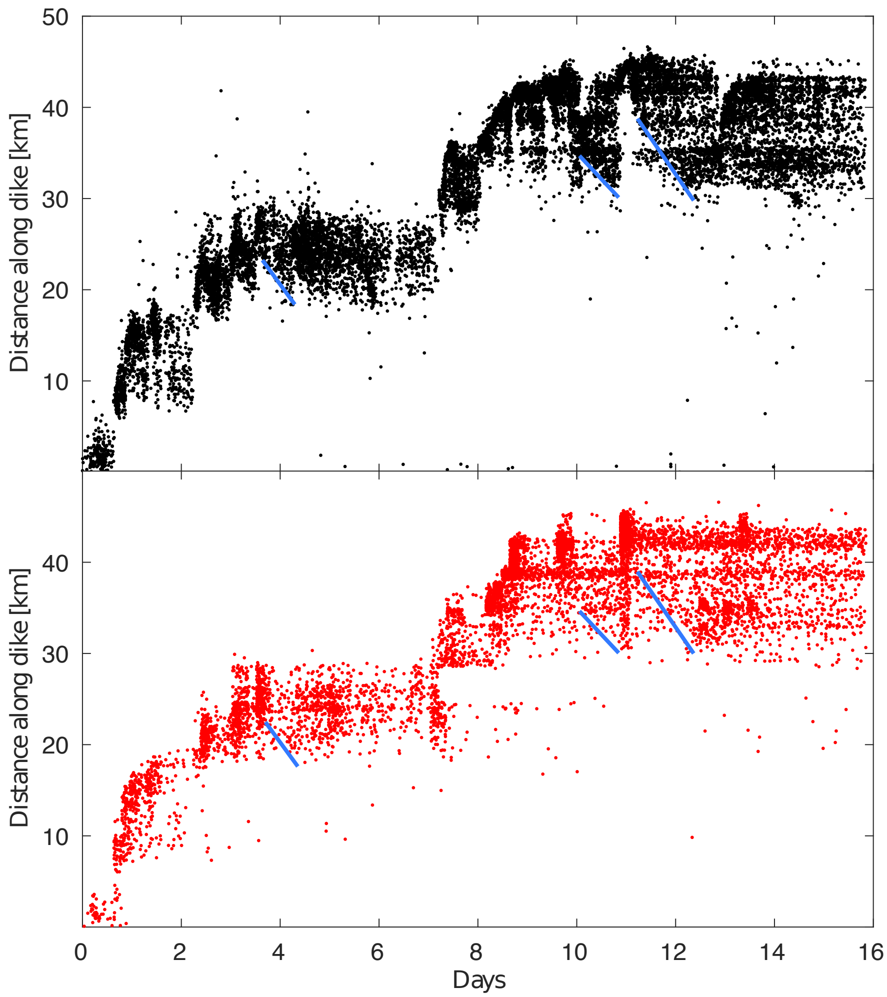

Figure 11. Comparison of observed and predicted seismicity interpreted in the form of individual events. Black dots show detected earthquakes, red dots are events simulated based on the MAP cumulative number of events. Blue lines indicates examples of back-propagation of seismicity and the corresponding locations in the predicted seismicity (see Section 4.2 for discussion of the back-propgation)

4 Discussion

4.1 Background seismicity rate

One of the most significant uncertainties in this study is the background seismicity rate in each voxel. Very few events had been previously detected in the area where the dike propagated. Does that mean the background seismicity rate is zero? One possible explanation is that it is very low, such that no events large enough to be detected had occurred. The temporary seismic network in the area during the intrusion was able to detect much smaller events than the permanent seismic network in Iceland (SIL network). However, the MCMC sampling suggests that most voxels have a background seismicity rate near the upper limit, set at one event per 50 years. If that is correct, it is unlikely that no events would have been detected before 2014. We thus favor the explanation that seismic sources were not sufficiently stressed to produce earthquakes, but once exposed to the large dike-induced stresses, these sources were driven to failure. We made some attempts at estimating this threshold using a non-constant background rate (equations 34 in *Heimisson and Segall* [2018]). Due to uncertainty in the dike tip location and the fact that the two models behave in the same way once the threshold is reached, these attempts did not seem to give meaningful results and generally predicted a negligible threshold. In contrast, if we had placed the dike tip slightly ahead of the swarm, then such a threshold would be required. We conclude that the dike and post rifting period release most of the inter-diking stresses leaving the crust in a low-stress state. Indeed, previous studies found the dike opening to agree well with the expected strain accumulation since the last intrusion [*Ruch et al.*, 2016]. The absence of background seismicity prior to the diking event does not negate the use of the modified Dieterich theory, provided that the stress changes due to the dike are sufficient to elevate the population well above steady state [*Heimisson and Segall*, 2018].

4.2 Segmentation of seismicity and back-propagation

The model reproduces the segmentation of the seismicity along the dike length, where the newest intruding segment remains seismically active until the next segment is formed with very few earthquakes in the previous segments (Figure 11). This behavior can be physically understood from Figure 7, where in general the pressure drops as the dike grows, although it increases transiently when the dike stalls. During a pause, the seismic sources are exposed to increasing stresses. The seismicity rate R depends on the integral of the stress kernel $K(t)$ (equation 4):

$$\frac{R}{r} = \frac{K(t)}{1 + \frac{\dot{s}_b}{A\sigma_0}\int_0^t K(t')dt'}, \tag{11}$$

which means that during the pauses the integral in the denominator increases and, in physical terms, the population develops a stress memory or threshold, and will not be significantly activated again unless the stress change becomes larger than before. In summary, as a segment intrudes the pressure increases and reaches a maximum before the next segment is formed. Because the pressure never sufficiently exceeds the previous maximum, the previous segments are not reactivated seismically. Stress memory (Kaiser–effect) has been identified in triggering of volcano-tectonic earthquakes [*Heimisson et al.*, 2015b]. In some parts of the dike, where abrupt changes in direction (or kinks) occur, there is also a significant stress rotation that affects the populations near the kink. For example, a very clear shutoff of seismicity occurs in the simulated catalog (Figure 11) around day 7.5 and distance 25–29 km. This abrupt shutoff is due to geometric effects near the kink, causing a stress shadow. However, in most other parts of the dike, the segmentation in seismicity is caused by the stress memory effect. It is worth noting that magma solidification may also play a role, by affecting the compliance of the dike to pressure changes by reducing the height of the magma column from solidification in the narrower lower and/or upper parts. However, solidification is not included in our model and is thus not needed to explain the large scale segmentation of the seismicity.

Another striking feature of the seismicity is several occurrences of backward propagations of seismicity with approximately constant speed. Three of these are marked in Figure 11. The simulated catalog shows some indications of such back-propagations at similar times. However, the trend is far less clear compared to the observed seismicity. This may be in part due to discretization in space and time, which limit the resolution of features that occur on smaller temporal and spatial scales.

We suggest that these features may also be explained by a stress memory effect, as the dike advances the pressure drops. From Figure 7 we estimate that this occurs at about $\sim$ 2 MPa/h. At the same time, the stress sensed by the populations of seismic sources drops approximately proportionally. Once the dike halts it begins re-pressurizing (at a rate of about $\sim$ 0.1 MPa/h) the seismic sources along the length of the dike will have experienced different peak stresses and will reactivate at different times. In order to test this hypothesis, we compute the seismicity rate for hypothetical populations that have been exposed to varying peak stress the decreases with propagation distance. Once a minimum value is reached, all populations are subject to the same slow re-pressurization (Figure 12). Due to the stress memory effect, the populations are reactivated at different times and together produce back-propagation of seismicity at a constant speed that is proportional to the re-pressurization rate. However, we acknowledge that further study of the back-propagation is needed, in particular, to exclude other potential explanations and to explore more direct comparison with data at finer spatial resolution.

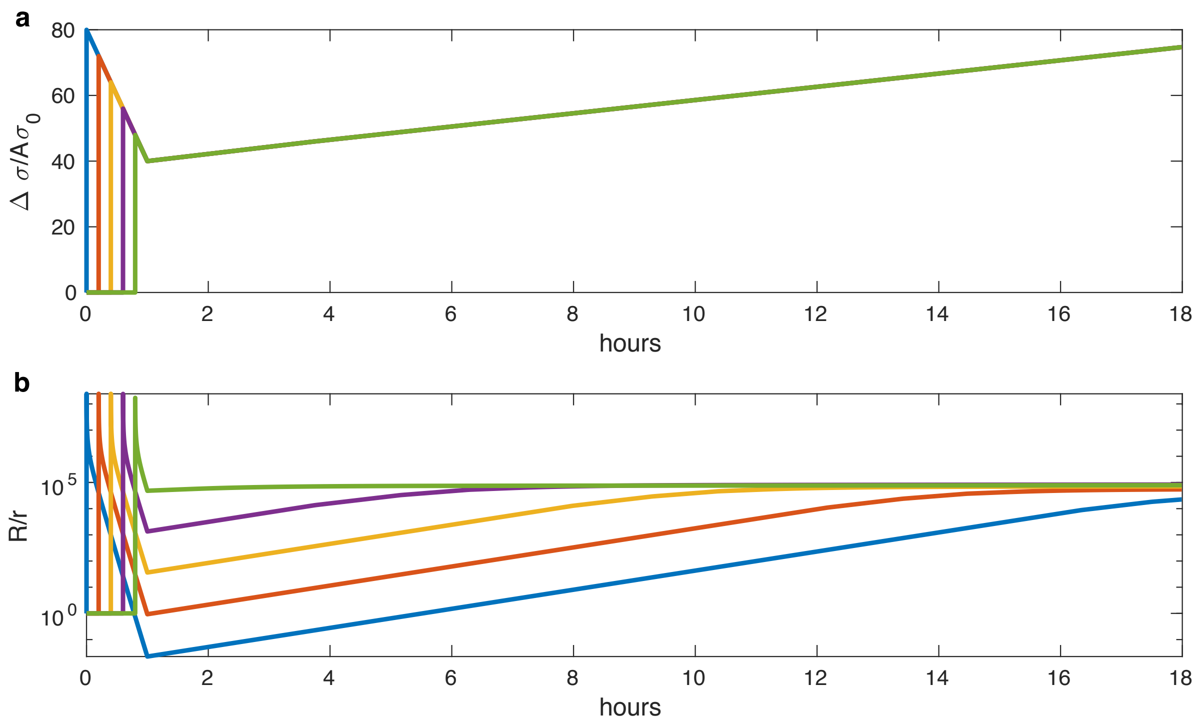

Figure 12. Idealized stressing histories (a) that may produce back-propagation of seismicity with constant speed. As the dike advances the pressure drops and thus the peak stress sensed by seismic sources decrease with migration distance (blue to green lines). Once the dike propagation halts, the slow depressurization begins, which will be approximately constant for all the seismic populations. Equation 11 reveals that each population of sources is only significantly reactivated once the stress reaches the previous peak value. The back-propagation rate should, therefore, be proportional to the re-pressurization rate.

It is generally agreed that the propagation of a dike induced seismic swarm results directly from the propagation and lengthening of the dike. We further suggest that many spatiotemporal complexities in the dike induced seismicity result largely from the interplay of time-dependent pressure and stress memory effects. As a consequence, seismicity is fairly insensitive to the absolute pressure in the dike, but the turning on and off of seismicity may indicate transient pressure changes, where seismicity rate increase rapidly upon exceeding previous pressure levels. In summary, the seismicity does not directly measure the current state of stress at a point in the crust but rather responds to the recent stressing history of that point. Additional information from geodetic measurements is, therefore, essential to deconvolve the stressing history and the observable seismicity.

4.3 Secondary triggering

Where the *Dieterich* [1994] theory has been used in a similar manner as in this study, it has been noted that there may be possible uncertainty due to source interactions and secondary events [*Segall et al.*, 2013; *Inbal et al.*, 2017]. This concern is motivated by the assumption in the Dieterich model that sources do not interact. Several algorithms and methods have been developed to deluster earthquakes and remove aftershocks or secondary events, but each method is based on different assumptions and they will generally produce different results when applied to the same catalog [*Marsan and Lengline*, 2008]. Moreover, most declustering methods are made to separate mainshocks from aftershocks that occur under slow tectonic loading, where most spatial and temporal clustering can be explained by the mainshock triggering the aftershocks. Dike intrusions are striking examples of extremely strong spatial and temporal clustering of earthquakes that are not primarily driven by mainshock - aftershock triggering, but by the time evolution of the stress field induced by the dike. Thus, it can be argued that most declustering methods are not appropriate for such a sequence. Furthermore, *Heimisson* [2019] challenged the view that declustering is required when applying the Dieterich model. He showed, under a few assumptions that hold fairly generally, that populations of seismic sources with and without interactions will produce the same seismicity rate when perturbed if they have the same background seismicity rate. This shows that a population with interactions can be approximated as a population without interactions with the same long term average background seismicity rate. In addition, *Heimisson* [2019] showed in simulations that interaction between populations, that arise in a spatially heterogeneous stress field, do not change the absolute number of events on a regional scale for time $t \gg t_a$. This suggests that interactions do not change the absolute number of events, although they may somewhat change the temporal and spatial distribution of them. The theoretical finding of *Heimisson* [2019] indicates that the assumption of non-interacting sources is not as consequential as it may seem. Given the discussion above, we assess that using the full seismic catalog introduces less bias than declustering, which may likely remove physically relevant spatial and temporal correlations in the seismicity.

4.4 Validation of the Dieterich model

Our results demonstrate the applicability of the Dieterich model to temporally complicated and large magnitude stress changes. The results show that the model is consistent with the cumulative number of events in most voxels even after independent observations such as GPS and InSAR have been used to constrain the complete stressing history in each voxel. In that sense, the results provide significant observational validation of the theory since the temporal evolution of the cumulative number of events is strongly controlled by stressing history. However, in order to match the observations, it is necessary to constrain time-independent parameters in each voxel, and some of those parameters must be spatially heterogeneous (Figure 9).

4.5 Further development of joint inversions for dike propagation

Segall et al. [2013] proposed that we may image a propagating dike through simultaneous joint inversion of both earthquakes and deformation, where deformation is sensitive to the inflation of the dike, but the earthquakes can better constrain the location of the dike tip. *Segall et al.* [2013] tested the method on the Father's day dike intrusion on Kilauea that had about 200 recorded earthquakes and managed to simultaneously fit the cumulative number of events and GPS time-series assuming spatially constant background stresses and frictional parameters. The results in this study demonstrate that fitting a voxel with a few events can be done for a wide range of parameters, but when the number of events exceeds about one hundred, the fit can only be achieved in a very narrow range in the model space. Performing such joint inversion for the 2014 Bárðarbunga dike would require accounting for the frictional structure in some stochastic manner since uniform frictional properties are not consistent with the observations. At the current time, we have not explored such joint inversions of the Bárðarbunga data with stochastic parameter distributions.

Looking ahead, the end goal of joint inversions of seismic and geodetic data to image a dike would be to do so in real-time. This task involves further challenges, in particular, related to the lack of knowledge of the dike path. In some places, dikes propagate along a rift zone, such that the path may be known reasonably beforehand, but because voxels should not intersect the dike plane that knowledge of the trajectory would need to be precise. In the more general case, the problem would require adaptive meshing that can follow the dike as it dike propagates that can follow its trajectory. An adaptive meshing would substantially increase the computational cost of the inversion.

5 Conclusions

We have developed a methodology where deformation and seismicity are analyzed using a single physics-based dike model in a fully consistent manner. The approach makes use of geodetic data (InSAR and GPS) and seismic data (earthquake locations and focal mechanism) to construct a dike model that predicts both deformation and seismicity. The model was applied to the spatially and temporally complicated 2014 Bárðarbung diking event. The results shed light on the physics of dike induced earthquakes, which are consistent with elastic stress transfer onto preexisting faults. Thus indicating that dike induced earthquakes are not caused by new fractures, but are triggered on faults as has previously been suggested [*Rubin and Gillard*, 1998]. Furthermore, the inversion of earthquake number provides a rare insight into the potential frictional structure of the crust, where constitutive parameters A and α, show considerable variability, but spatial correlation. The correlation is not imposed through spatial smoothing and may suggest robustness of the inversion process and methodology. The application of the modified Dieterich theory [*Heimisson and Segall*, 2018] shown here serves as a new test of its applicability. Where we have not only applied it to a more complicated stressing history than previous studies but also applied to a new volcano-tectonic setting. The GPS inversion indicates that on average pressure drops in the dike although it is temporarily elevated while the dike stalls. This may explain the characteristic segmentation of the Bárðarbung dike, which is captured by the model, as a manifestation of a stress threshold or memory effect, because the pressure never becomes sufficiently large to reactive the previous segments.

Acknowledgments

We thank Tim Greenfield, Bob White and Thorbjörg Águstsdóttir for providing access to earthquake locations and magnitude estimates prior to publication. We also thank Sigrún Hreinsdóttir for providing the 8h GPS time series and Andy Hooper for the processed and downsampled interferograms. All data used in this study can be found under following references [*Sigmundsson et al.*, 2015; *Greenfield et al.*, 2018; *Ágústsdóttir et al.*, 2019]. This research was supported by: NASA under the NASA Earth and Space Science Fellowship Program - Grant NNX16AO40H, and NASA ROSES ESI - Grant NNX16AN08G.

References

Ágústsdóttir, T., J. Woods, T. Greenfield, R. G. Green, R. S. White, T. Winder, B. Brandsdóttir, S. Steinthórsson, and H. Soosalu (2016), Strike-slip faulting during the 2014 Bárðarbunga-Holuhraun dike intrusion, central Iceland, *Geophysical Research Letters*, *43*(4), 1495–1503, doi:10.1002/2015GL067423.

Ágústsdóttir, T., J. Woods, T. Winder, R. S. White, T. Greenfield, and B. Brandsdóttir (2019), Intense seismicity during the 2014–15 bárðarbunga–Holuhraun rifting event, Iceland, reveals the nature of dike-induced earthquakes and caldera collapse mechanisms, *Journal of Geophysical Research: Solid Earth*, doi:10.1029/2018JB016010.

Árnadóttir, Þ., W. Jiang, K. L. Feigl, H. Geirsson, and E. Sturkell (2006), Kinematic models of plate boundary deformation in southwest Iceland derived from GPS observations, *Journal of Geophysical Research: Solid Earth*, *111*(B7), doi:10.1029/2005JB003907.

Audet, C., and J. E. Dennis Jr (2002), Analysis of generalized pattern searches, *SIAM Journal on Optimization*, *13*(3), 889–903.

Blanpied, M., D. Lockner, and J. Byerlee (1991), Fault stability inferred from granite sliding experiments at hydrothermal conditions, *Geophysical Research Letters*, *18*(4), 609–612.

Brandsdottir, B., and P. Einarsson (1979), Seismic activity associated with the september 1977 deflation of the krafla central volcano in northeastern iceland, *Journal of Volcanology and Geothermal Research*, *6*(3-4), 197–212.

Carlson, R. L., and C. N. Herrick (1990), Densities and porosities in the oceanic crust and their variations with depth and age, *Journal of Geophysical Research: Solid Earth*, *95*(B6), 9153–9170, doi:10.1029/JB095iB06p09153.

Cayol, V., and F. H. Cornet (1998), Three-dimensional modeling of the 1983–1984 eruption at Piton de la Fournaise Volcano, Réunion Island, *Journal of Geophysical Research: Solid Earth*, *103*(B8), 18,025–18,037, doi:10.1029/98JB00201.

Christensen, N. I., and R. H. Wilkens (1982), Seismic properties, density, and composition of the Icelandic crust near Reydarfjörður, *Journal of Geophysical Research: Solid Earth*, *87*(B8), 6389–6395, doi:10.1029/JB087iB08p06389.

Dieterich, J. (1994), A constitutive law for rate of earthquake production and its application to earthquake clustering, *Journal of Geophysical Research: Solid Earth*, *99*(B2), 2601–2618, doi:10.1029/93JB02581.

Drouin, V., F. Sigmundsson, B. G. Ófeigsson, S. Hreinsdóttir, E. Sturkell, and P. Einarsson (2017), Deformation in the Northern Volcanic Zone of Iceland 2008–2014: An interplay of tectonic, magmatic, and glacial isostatic deformation, *Journal of Geophysical Research: Solid Earth*, *122*(4), 3158–3178, doi: 10.1002/2016JB013206.

Du, Y., and A. Aydin (1992), Three-dimensional characteristics of dike intrusion along the northern Iceland Rift from inversion of geodetic data, *Tectonophysics*, *204*(1), 111–121, doi:10.1016/0040-1951(92)90273-9.

Fialko, Y. A., and A. M. Rubin (1999), What controls the along-strike slopes of volcanic rift zones?, *Journal of Geophysical Research: Solid Earth*, *104*(B9), 20,007–20,020, doi:10.1029/1999JB900143.

Foreman-Mackey, D., D. W. Hogg, D. Lang, and J. Goodman (2013), emcee: the MCMC hammer, *Publications of the Astronomical Society of the Pacific*, *125*(925), 306.

Goldberg, D. E., and J. H. Holland (1988), Genetic algorithms and machine learning, *Machine learning*, *3*(2), 95–99.

Goodman, J., and J. Weare (2010), Ensemble samplers with affine invariance, *Communications in applied mathematics and computational science*, *5*(1), 65–80.

Green, R. G., T. Greenfield, and R. S. White (2015), Triggered earthquakes suppressed by an evolving stress shadow from a propagating dyke, *Nature Geoscience*, *8*(8), 629–632, doi:10.1038/ngeo2491.

Greenfield, T., R. S. White, T. Winder, and T. Ágústsdóttir (2018), Seismicity of the askja and bárðarbunga volcanic systems of Iceland, 2009–2015, *Journal of Volcanology and Geothermal Research*, doi:10.1016/j.jvolgeores.2018.08.010.

Guðmundsson, M. T., and Þ. Högnadóttir (2007), Volcanic systems and calderas in the Vatnajökull region, Central Iceland: Constraints on crustal structure from gravity data, *Journal of Geodynamics*, *43*(1), 153–169, doi: 10.1016/j.jog.2006.09.015, hotspot Iceland.

Hainzl, S., S. Steacy, and D. Marsan (2010), Seismicity models based on Coulomb stress calculations, Community Online Resource forStatistical Seismicity Analysis, doi:10.5078/corssa-32035809. [Available at http://www.corssa.org.]

Hartley, M. E., and T. Thordarson (2013), The 1874–1876 volcano-tectonic episode at Askja, North Iceland: Lateral flow revisited, *Geochemistry, Geophysics, Geosystems*, *14*(7), 2286–2309.

Heimisson, E. R. (2019), Constitutive law for earthquake production based on rate-and-state friction: Theory and application of interacting sources, *Journal of Geophysical Research: Solid Earth*, *124*(2), 1802–1821, doi:10.1029/2018JB016823.

Heimisson, E. R., and P. Segall (2018), Constitutive law for earthquake production based on rate-and-state friction: Dieterich 1994 revisited, *Journal of Geophysical Research: Solid Earth*, *123*(5), 4141–4156, doi:10.1029/2018JB015656.

Heimisson, E. R., A. Hooper, and F. Sigmundsson (2015a), Forecasting the path of a laterally propagating dike, *Journal of Geophysical Research: Solid Earth*, doi:10.1002/2015JB012402.

Heimisson, E. R., P. Einarsson, F. Sigmundsson, and B. Brandsdottir (2015b), Kilometer-scale kaiser effect identified in Krafla volcano, Iceland, *Geophysical Research Letters*, *42*(19), 7958–7965, doi:10.1002/2015GL065680.

Hooper, A., B. Ófeigsson, F. Sigmundsson, B. Lund, P. Einarsson, H. Geirsson, and E. Sturkell (2011), Increased capture of magma in the crust promoted by ice-cap retreat in Iceland, *Nature Geoscience*, *4*(11), 783–786, doi:10.1038/ngeo1269.

Inbal, A., J.-P. Ampuero, and J.-P. Avouac (2017), Locally and remotely triggered aseismic slip on the central san jacinto fault near Anza, CA, from joint inversion of seismicity and strainmeter data, *Journal of Geophysical Research: Solid Earth*, *122*(4), 3033–3061, doi:10.1002/2016JB013499.

Jónsson, S., H. Zebker, P. Cervelli, P. Segall, H. Garbeil, P. Mouginis-Mark, and S. Rowland (1999), A shallow-dipping dike fed the 1995 flank eruption at Fernandina volcano, Galapagos, observed by satellite radar interferometry, *Geophysical Research Letters*, *26*(8), 1077–1080, doi:10.1029/1999GL900108.

Key, J., R. S. White, H. Soosalu, and S. S. Jakobsdóttir (2011), Multiple melt injection along a spreading segment at Askja, Iceland, *Geophysical Research Letters*, *38*(5), doi:10.1029/2010GL046264, l05301.

LaFemina, P. C., T. H. Dixon, R. Malservisi, Þ. Árnadóttir, E. Sturkell, F. Sigmundsson, and P. Einarsson (2005), Geodetic GPS measurements in south Iceland: Strain accumulation and partitioning in a propagating ridge system, *Journal of Geophysical Research: Solid Earth*, *110*(B11), doi:10.1029/2005JB003675, b11405.

Larsen, G., and K. Grönvold (1979), Volcanic eruption through a geothermal borehole at Namafjall, Iceland, *Nature*, *278*, 707–710.

Linker, M. F., and J. H. Dieterich (1992), Effects of variable normal stress on rock friction: Observations and constitutive equations, *Journal of Geophysical Research: Solid Earth*, *97*(B4), 4923–4940, doi:10.1029/92JB00017.

Marsan, D., and O. Lengline (2008), Extending earthquakes' reach through cascading, *Science*, *319*(5866), 1076–1079.

Okada, Y. (1992), Internal deformation due to shear and tensile faults in a half-space, *Bulletin of the Seismological Society of America*, *82*(2), 1018–1040.

Parks, M. M., E. R. Heimisson, F. Sigmundsson, A. Hooper, K. S. Vogfjörd, T. Árnadóttir, B. Ófeigsson, S. Hreinsdóttir, Á. R. Hjartardóttir, P. Einarsson, et al. (2017), Evolution of deformation and stress changes during the caldera collapse and dyking at Bárdarbunga, 2014–2015: Implication for triggering of seismicity at nearby Tungnafellsjökull volcano, *Earth and Planetary Science Letters*, *462*, 212–223, doi:10.1016/j.epsl.2017.01.020

Rubin, A. M. (1993), Tensile fracture of rock at high confining pressure: Implications for dike propagation, *Journal of Geophysical Research: Solid Earth*, *98*(B9), 15,919–15,935, doi:10.1029/93JB01391.

Rubin, A. M., and D. Gillard (1998), Dike-induced earthquakes: Theoretical considerations, *Journal of Geophysical Research: Solid Earth*, *103*(B5), 10,017–10,030, doi:10.1029/97JB03514.

Ruch, J., T. Wang, W. Xu, M. Hensch, and S. Jónsson (2016), Oblique rift opening revealed by reoccurring magma injection in central Iceland, *Nature communications*, *7*, doi:10.1038/ncomms12352.

Savage, J. C., and R. O. Burford (1973), Geodetic determination of relative plate motion in central California, *Journal of Geophysical Research*, *78*(5), 832–845, doi:10.1029/JB078i005p00832.

Segall, P., A. L. Llenos, S.-H. Yun, A. M. Bradley, and E. M. Syracuse (2013), Time-dependent dike propagation from joint inversion of seismicity and deformation data, *Journal of Geophysical Research: Solid Earth*, *118*(11), 5785–5804, doi:10.1002/2013JB010251.

Sigmundsson, F., S. Hreinsdóttir, A. Hooper, Þ. Árnadóttir, R. Pedersen, M. J. Roberts, N. Óskarsson, A. Auriac, J. Decriem, P. Einarsson, H. Geirsson, M. Hensch, B. G. Öfeigsson, E. Sturkell, H. Sveinbjörnsson, and K. L. Feigl (2010), Intrusion triggering of the 2010 Eyjafjallajokull explosive eruption, *Nature*, *468*(7322), 426–430, doi:10.1038/nature09558.

Sigmundsson, F., A. Hooper, S. Hreinsdottir, K. S. Vogfjörð, B. G. Ófeigsson, E. R. Heimisson, S. Dumont, M. Parks, K. Spaans, G. B. Guðmundsson, V. Drouin, Þ. Árnadóttir, K. Jónsdóttir, M. T. Guðmundsson, Þ. Högnadóttir, H. M. Friðriksdóttir, M. Hensch, P. Einarsson, E. Magnússon, S. Samsonov, B. Brandsdóttir, R. S. White, Þ. Ágústsdóttir, T. Greenfield, R. G. Green, Á. R. Hjartardóttir, R. Pedersen, R. A. Bennett, H. Geirsson, P. C. La Femina, H. Björnsson, F. Pálsson, E. Sturkell, C. J. Bean, M. Mollhoff, A. K. Braiden, and E. P. S. Eibl (2015), Segmented lateral dyke growth in a rifting event at Bardarbunga volcanic system, Iceland, *Nature*, *517*(7533), 191–195, doi:10.1038/nature14111, letter.

Soosalu, H., J. Key, R. White, C. Knox, P. Einarsson, and S. S. Jakobsdóttir (2010), Lower-crustal earthquakes caused by magma movement beneath Askja volcano on the north Iceland rift, *Bulletin of Volcanology*, *72*(1), 55–62, doi:10.1007/s00445-009-0297-3.

Spaans, K., and A. Hooper (2018), Insights into the stress field around Bár arbunga volcano from the 2014/2015 Holuhraun rifting event, *Journal of Geophysical Research: Solid Earth*, *123*(4), 3238–3249, doi:10.1002/2017JB015274.

Sparks, R., P. Meyer, and H. Sigurdsson (1980), Density variation amongst mid-ocean ridge basalts: Implications for magma mixing and the scarcity of primitive lavas, *Earth and Planetary Science Letters*, *46*(3), 419–430.

Sturkell, E., and F. Sigmundsson (2000), Continuous deflation of the Askja caldera, Iceland, during the 1983–1998 noneruptive period, *Journal of Geophysical Research: Solid Earth*, *105*(B11), 25,671–25,684, doi:10.1029/2000JB900178.

Townsend, M. R., D. D. Pollard, and R. P. Smith (2017), Mechanical models for dikes: A third school of thought, *Tectonophysics*, *703–704*, 98–118, doi:10.1016/j.tecto.2017.03.008.

Supporting Information for
"Fully consistent modeling of dike induced deformation and seismicity: Application to the 2014 Bárðarbunga dike, Iceland"

Elías R. Heimisson[1], **Paul Segall**[1]

[1]Department of Geophysics, Stanford University, Stanford, California, USA

Contents

Additional Supporting Information (Files uploaded separately)

1. Captions for Movies S1

Introduction

This supplement contains three additional figures S1, S2 and S3 that help characterize the statistical properties and uncertainty from the MCMC sampling that is presented in the main manuscript. Furthermore, the supplement contains a caption for a movie file (.avi) which shows that dike model opening with time and both cumulative observed (gray) and model predicted earthquakes (blue).

Corresponding author: Elías R. Heimisson, `eliasrh@stanford.edu`

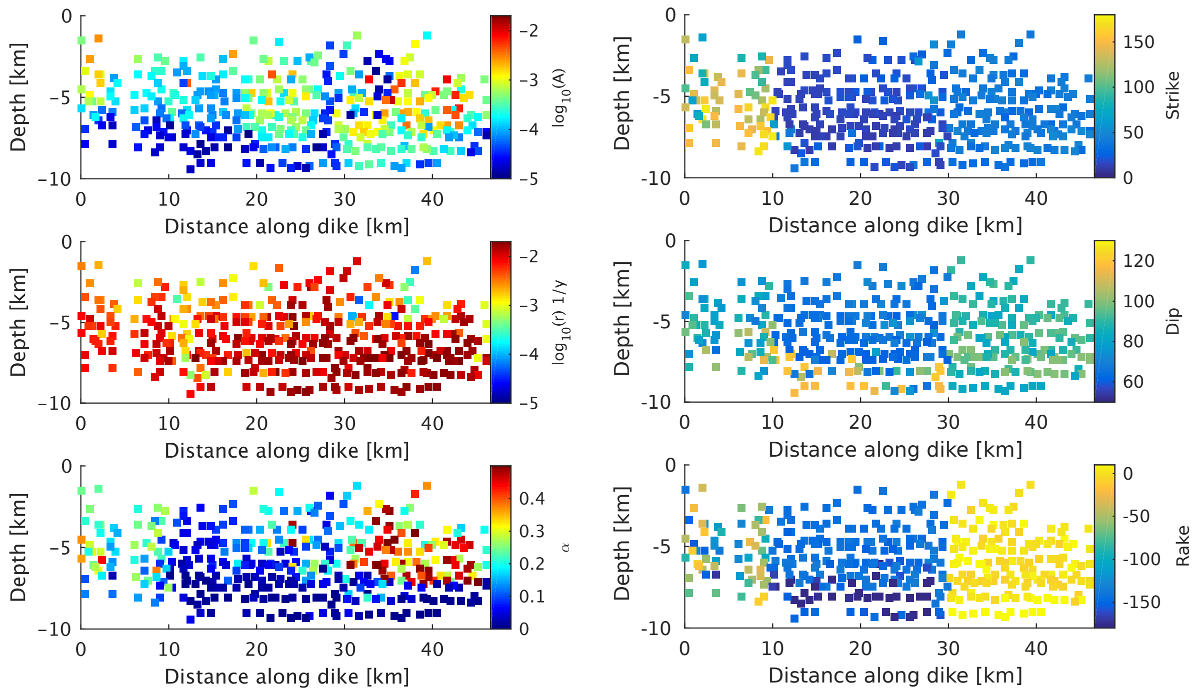

Figure S1. Median value from MCMC sampling of each parameter in each voxel. The median may not correspond to a highly probable set of model parameters due to the theory being strongly nonlinear and the distributions tend to be multimodal.

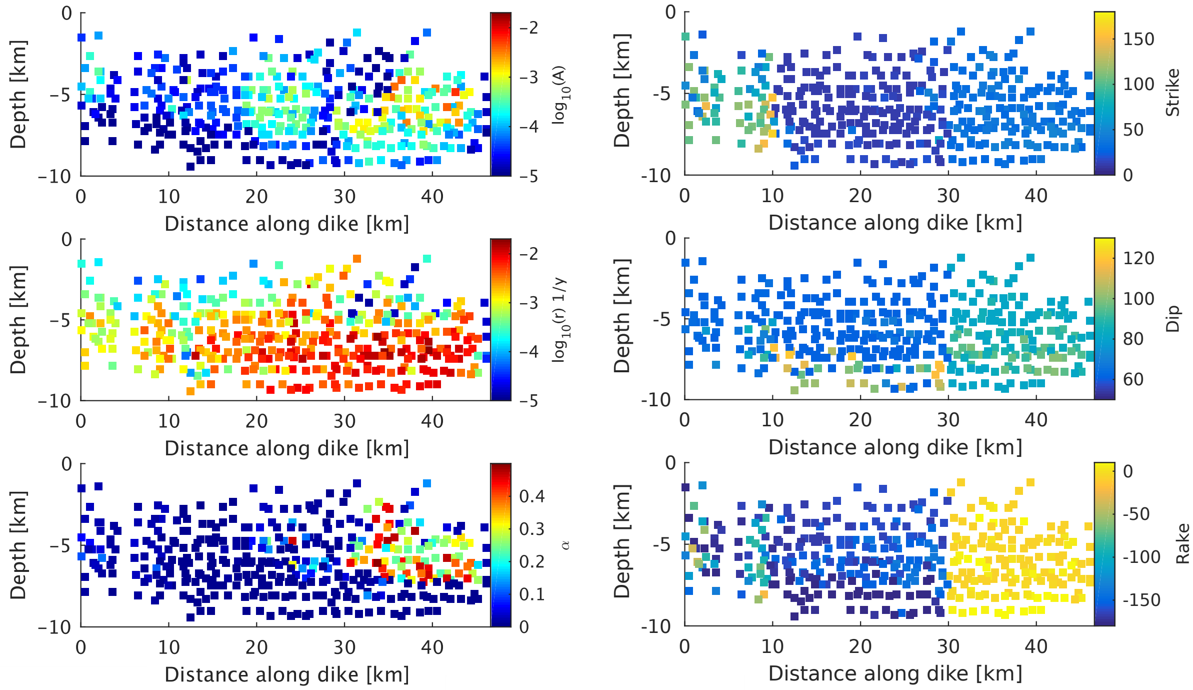

Figure S2. The 5th percentile values from the MCMC sampling of each parameter in each voxel. These values may be regarded as a lower bound of the probable range of model parameters.

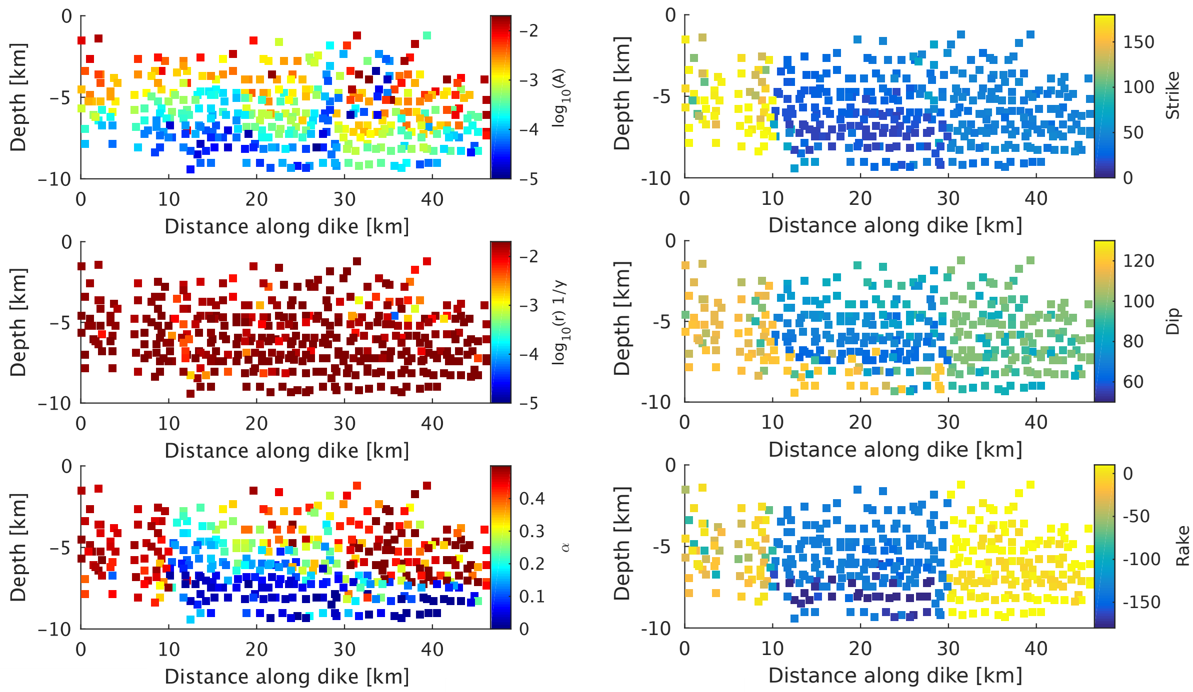

Figure S3. The 95th percentile values from the MCMC sampling of each parameter in each voxel. These values may be regarded as an upper bound of the probable range of model parameters.

Movie S1.

Dike opening at fixed time steps, top: observed cumulative number of events, bottom: model predicted cumulative number of events. Note that triangular structures that appear in the predicted cumulative number of events are artifacts of the voxel discretization.